

**Notice:**

This manuscript has been resubmitted to Geochemistry, Geophysics, Geosystems following peer review. Subsequent versions may differ in text and content, please check for the newest version before referencing this preprint.

**Details:**

Title: Lateral variations in lower crustal strength control the temporal evolution of mountain ranges: examples from south-east Tibet

## Authors:

Camilla Penney (COMET, University of Cambridge)

Alex Copley (COMET, University of Cambridge)

Contact: [cp451@cam.ac.uk](mailto:cp451@cam.ac.uk)

1 Lateral variations in lower crustal strength control the  
2 temporal evolution of mountain ranges: examples from  
3 south-east Tibet

4 Camilla Penney<sup>1\*</sup>, Alex Copley<sup>1</sup>

5 July 1, 2020

6 Key points:

- 7 • Lateral variations in lower crustal strength provide a first-order control on the shape  
8 and temporal evolution of mountain ranges.
- 9 • Strong lower crust in the Sichuan Basin can explain the development of topography in  
10 the Longmen Shan without a lower crustal channel.
- 11 • Lateral transport of samples should be considered in calculating and interpreting  
12 palaeoelevations from stable-isotope palaeoaltimetry.

---

\*Corresponding author: cp451@cam.ac.uk, <sup>1</sup>COMET, Bullard Laboratories, Department of Earth Sciences, University of Cambridge, Cambridge, UK

## 13 **Abstract**

14 Controversy surrounds the rheology of the continental lithosphere, and how it controls the  
15 evolution and behaviour of mountain ranges. In this study, we investigate the effect of lat-  
16 eral contrasts in the strength of the lower crust, such as those between cratonic continental  
17 interiors and weaker rocks in the adjacent deforming regions, on the evolution of topogra-  
18 phy. We combine numerical modelling with recently published results from stable-isotope  
19 palaeoaltimetry in south-east Tibet. Stable-isotope palaeoaltimetry in this region provides  
20 constraints on vertical motions, which are required to distinguish between competing mod-  
21 els for lithosphere rheology and deformation. We use numerical modelling to investigate the  
22 effect of lateral strength contrasts on the shape and temporal evolution of mountain ranges.  
23 In combination with palaeoaltimetry results, our modelling suggests that lateral strength  
24 contrasts provide a first-order control on the evolution of topography in south-east Tibet.  
25 We find that the evolution of topography in the presence of such strength contrasts leads  
26 to laterally-varying topographic gradients, and to key features of the GPS- and earthquake-  
27 derived strain-rate field, without the need for a low-viscosity, lower-crustal channel. We  
28 also find that palaeoaltimetric samples may have been transported laterally for hundreds  
29 of kilometres, an effect which should be accounted for in their interpretation. Our results  
30 are likely to be applicable to the evolution of mountain ranges in general, and provide an  
31 explanation for the spatial correlation between cratonic lowland regions and steep mountain  
32 range-fronts.

## 33 **Plain Language Summary**

34 The rocks which make up the Earth's continents move and change shape in response to  
35 tectonic forces. How rocks respond to these forces depends on their material properties,  
36 and can vary in space and time. These material properties, therefore, control the shape

37 of mountain ranges and how mountains grow. This study investigates why some mountain  
38 ranges have steep fronts, whilst others have gentle gradients. We look at how regions made  
39 up of strong rocks (such as the Sichuan Basin) affect the shape and growth of adjacent  
40 mountain ranges. We find that mountain ranges with steep fronts can form when weaker  
41 rocks move over stronger ones. Recent measurements of oxygen in ancient soils suggests that  
42 parts of the south-eastern margin of the Tibetan Plateau (between the Sichuan Basin and  
43 the Central Lowlands of Myanmar) have been high since about 50 million years ago, and  
44 that the area has risen more slowly than has previously been estimated. In south-east Tibet,  
45 the pattern of earthquakes, and how fast the mountains have grown, can be explained by  
46 these strong areas, without invoking complicated material properties in the mountain ranges.  
47 Such strong regions may be important in controlling the shape of mountain ranges globally.

## 48 **1 Introduction**

49 The strength of the lithosphere provides a first-order control on the distribution of strain  
50 within it. Strength, here, means resistance to deformation, which might be controlled by  
51 the stresses transmitted across faults in the brittle part of the lithosphere or the rheology  
52 associated with ductile creep in the mid-to-lower crust and upper mantle. Lateral strength  
53 contrasts, such as those between anhydrous rocks in cratonic continental interiors (from  
54 which volatiles have been removed by previous partial melting) and more hydrous rocks  
55 in the adjacent deforming regions, are a feature of continental lithosphere globally. Such  
56 contrasts control the distribution of strain in the continents and, therefore, the evolution of  
57 mountain ranges (e.g. Vilotte et al., 1984; England and Houseman, 1985; Flesch et al., 2001;  
58 Jackson et al., 2008). Regions with strong crust, such as cratons, tend to accommodate little  
59 strain in comparison to their surroundings. In the India–Eurasia collision, for example, the  
60 accreted terranes which form the southern margin of Eurasia, rather than cratonic India,

61 have accommodated most of the shortening. Here we investigate the effect of lateral con-  
62 trasts in the strength of the lower crust on the temporal evolution of mountain belts.

63

64 A key outstanding question about the effect of lateral strength contrasts is how regions  
65 with strong lower crust, and the flow of less viscous material over and around them, affect the  
66 evolution of mountain ranges over tens of millions of years. Previous studies of continental  
67 deformation demonstrate that models which are able to reproduce instantaneous strain rates  
68 do not necessarily lead to the formation of the observed topography over time (e.g. Houseman  
69 and England, 1986; England and Houseman, 1986), so incorporating temporal evolution is an  
70 important extension to models considering the geologically-instantaneous effects of strength  
71 contrasts (e.g. Copley, 2008; Bischoff and Flesch, 2019). This paper concerns the physical  
72 controls on mountain building, and the constraints which recently-published stable-isotope  
73 palaeoaltimetry observations can provide on lithosphere rheology. Vertical motions, to which  
74 palaeoaltimetry observations are sensitive, have the potential to distinguish between rheolog-  
75 ical models which lead to the same horizontal surface velocities (Copley, 2008; Flesch et al.,  
76 2018). Understanding the implications of these observations, and the associated caveats is,  
77 therefore, critical to constraining lithosphere rheology. Numerical models with a small num-  
78 ber of parameters allow us to test whether lower-crustal strength contrasts, consistent with  
79 observations, can reproduce lateral variations in topographic gradients, or whether other  
80 driving mechanisms are required. In this study, we combine recently-published palaeoal-  
81 timetry observations from south-east Tibet, with a simple 3D model of crustal deformation,  
82 to explore the effects of lateral strength contrasts in controlling continental deformation.

83

84 The south-eastern margin of the Tibetan plateau (south-east Tibet, Figure 1) is a good  
85 place to study the effect of lateral strength contrasts. Low elevations, relief and strain rates  
86 (both seismic – Figure 1 – and geodetic – Zheng et al., 2017; Maurin et al., 2010) in the

87 Sichuan Basin and the Central Lowlands of Myanmar suggest that these regions experience  
88 relatively little deformation. These regions are, therefore, likely to be strong in comparison  
89 to the high region between them, and the mountain belts which surround them, which have  
90 undergone significant recent and cumulative deformation. The Sichuan Basin is covered  
91 by  $\sim 10$  km of sediments (Hubbard and Shaw, 2009), underlain by Paleoproterozoic crust  
92 (Burchfiel et al., 1995) with high seismic velocities in the upper mantle (e.g. Lebedev and  
93 Nolet, 2003; Li and Van Der Hilst, 2010). Post-seismic motion after the 2008 Wenchuan  
94 earthquake suggests a strength contrast across the Longmen Shan (Huang et al., 2014), as  
95 do differences in elastic thickness between the Longmen Shan and the Sichuan Basin esti-  
96 mated from gravity anomalies (Fielding and McKenzie, 2012).

97

98 Although the Central Lowlands of Myanmar have been less extensively studied than the  
99 Longmen Shan, the lack of topography, and the presence of undeformed Miocene sediments  
100 suggest low rates of post-Miocene deformation (Wang et al., 2014). Initial GPS measure-  
101 ments by Maurin et al. (2010) suggest that central Myanmar, west of the Sagaing fault,  
102 deforms in a coherent manner. Earthquakes in the Central Lowlands of Myanmar, shown in  
103 Figure 1b, are associated either with strike-slip motion on the Sagaing fault, on the eastern  
104 margin of the lowlands (which accommodates a component of the oblique India–Eurasia con-  
105 vergence; Maurin et al., 2010) or with active subduction beneath the Indo-Burman ranges  
106 (e.g. Stork et al., 2008; Steckler et al., 2016, yellow focal mechanisms in Figure 1b have  
107 depths  $> 50$  km). The seismic strain rate within the Central Lowlands is, therefore, low, at  
108 least in the instrumental period.

109

110 In contrast, the high regions of south-east Tibet deform rapidly, with kinematics de-  
111 scribed in detail by Copley (2008), who also summarised the work of previous authors. Since  
112 that study, numerous thrust-faulting earthquakes have occurred along the Longmen Shan,

113 including the 2008 Wenchuan and 2013 Lushan earthquakes and their aftershocks (Figure 1).  
114 These earthquakes, and subsequent analysis of shortening on structures imaged in seismic  
115 profiles (Hubbard and Shaw, 2009), demonstrate that active shortening of the brittle upper  
116 crust is occurring across the Longmen Shan.

117

118 Much of the morphology of south-east Tibet is dominated by deeply-incised river valleys,  
119 often following strike-slip faults (Wang and Burchfiel, 1997). Collectively these strike-slip  
120 faults accommodate south-eastwards motion of high topography relative to both the Sichuan  
121 Basin and the Central Lowlands of Myanmar (e.g. Shen et al., 2005), with the faults on op-  
122 posite sides of the high region accommodating opposite senses of shear (Figure 1a). The  
123 Xianshuihe and Sagaing faults (Figure 1a) have left- and right-lateral geodetic slip rates of  
124  $\sim 7\text{--}9\text{ mm yr}^{-1}$  and  $\sim 18\text{ mm yr}^{-1}$  respectively (Zheng et al., 2017; Maurin et al., 2010).  
125 The region of distributed left-lateral faulting east of the Sagaing fault (Figure 1a) accom-  
126 modates right-lateral shear on north-south striking planes through rotations about vertical  
127 axes (Copley, 2008).

128

129 A suite of models (e.g. Royden et al., 1997; Clark and Royden, 2000; Clark et al., 2005a;  
130 Burchfiel et al., 2008) have focussed on the possibility of flow in a low viscosity, lower-crustal  
131 channel producing the steep topography of the Longmen Shan, and the gentle topographic  
132 gradients to the south of the basin. By extending these channel-flow models to include rigid  
133 regions, Cook and Royden (2008) argued for the importance of both a strong Sichuan Basin  
134 and flow in a mid-lower crustal channel, in the formation of steep topography across the  
135 Longmen Shan. Chen et al. (2013a) and Chen et al. (2013b) used 2D thermo-mechanical  
136 models with extrapolated laboratory flow laws to demonstrate that the craton was an im-  
137 portant control on deformation in the region. We build up on this work by using a simple  
138 3D model to isolate the effects of this rigid, cratonic region, and by comparing the results to

139 observational constraints from palaeoaltimetry.

140

141 Vertical velocities can distinguish between competing models of depth-dependent rheol-  
142 ogy which would lead to the same horizontal velocities (Copley, 2008; Flesch et al., 2018;  
143 Bischoff and Flesch, 2019). Copley (2008) demonstrated that rapid flow at depth associated  
144 with a weak mid-to-lower crust would lead to faster instantaneous vertical motions than  
145 coherent upper- and lower- crustal deformation. The specific rates were based on instanta-  
146 neous calculations, so would not necessarily apply to the geologically-recorded uplift rates,  
147 but exemplify the possibility of using vertical motions to distinguish between different mod-  
148 els of depth-dependent rheology.

149

150 Previous quantitative studies of topographic evolution in south-east Tibet have focussed  
151 on thermochronology (e.g. Kirby et al., 2002; Clark et al., 2004; Wang et al., 2012, 2016).  
152 Thermochronometric ages give information about exhumation, which is controlled by the in-  
153 terplay between tectonics and erosion. Such ages have been interpreted to imply that rapid  
154 uplift occurred  $\sim 13\text{--}5$  Ma, based on the identification of geomorphic surfaces presumed to  
155 have formed at low elevation (Clark et al., 2005a, 2006). However, it has been suggested  
156 that such low-relief, erosional surfaces can also form at high elevations (e.g. Liu-Zeng et al.,  
157 2008; Yang et al., 2015) and that increased exhumation may have been related to changes in  
158 the base level of rivers draining the region (e.g. Richardson et al., 2008). The interpretation  
159 of the existing thermochronometric data in terms of elevation history is therefore unclear. In  
160 this study we make use of recently-published estimates of palaeoelevation from stable-isotope  
161 geochemistry, which provide an opportunity to quantitatively constrain the elevation history  
162 of south-east Tibet and, therefore, to distinguish between competing models of lithosphere  
163 rheology and mountain-range evolution.

164



165 We first summarise recently-published results from stable-isotope palaeoaltimetry (Sec-  
166 tion 2) to constrain the uplift and elevation history of south-east Tibet. We then use fluid-  
167 dynamical modelling of the mountain range (described in Section 3) to investigate the effects  
168 of lateral strength contrasts on the evolution of topography through time, and compare our  
169 results to south-east Tibet (Section 4).

170

171 Although the results presented here are in the context of south-east Tibet, the presence of  
172 lateral strength contrasts is a common feature of mountain ranges globally (e.g. Lamb, 2000;  
173 Jackson et al., 2008; Dayem et al., 2009b,a; Nissen et al., 2011). In particular, many moun-  
174 tain ranges, both active and older, have edges adjacent to cratons (McKenzie and Priestley,  
175 2008). – regions of (often thick) continental lithosphere, usually composed of Proterozoic  
176 or Archean crust, which have remained relatively undeformed by tectonic events on their  
177 margins (Holmes, 1965). In section 5, therefore, we discuss the applicability of our results  
178 to the temporal evolution of mountain ranges in general.

179

## 180 **2 Palaeoaltimetry**

181 Stable-isotope palaeoaltimetry uses systematic variations in the isotopic composition of pre-  
182 cipitation with elevation to derive the palaeoelevation of sample sites (e.g. Rowley et al.,  
183 2001). These techniques have been developed in order to place quantitative constraints on  
184 the elevation history of orogenies, such as Tibet, but they have not yet been extensively  
185 used as a constraint in dynamic models. South-east Tibet is a good region to carry out  
186 palaeoaltimetry studies. Moisture paths from the ocean to high topography in the region are  
187 simple, as the Rayleigh fractionation relationship between the oxygen-isotope composition  
188 of precipitation and elevation in present-day elevation transects shows (Hren et al., 2009).

189

190 Figure 2 shows results from seven recent palaeoaltimetry studies in south-east Tibet,  
191 which use soil-deposited (Hoke et al., 2014; Xu et al., 2016; Tang et al., 2017; Gourbet et al.,  
192 2017; Xiong et al., 2020) or lacustrine (Li et al., 2015; Xu et al., 2016; Gourbet et al., 2017; Wu  
193 et al., 2018) carbonates to derive the oxygen-isotope composition of palaeo-precipitation and,  
194 hence, palaeoelevations. In south-east Tibet, the age of sampled formations is a significant  
195 source of uncertainty (Hoke, 2018). Gourbet et al. (2017) and Li et al. (2020) have recently  
196 revised the ages of formations in the Jianchuan and Lühe basins respectively (Figure 2b).  
197 In the most extreme cases, more precise, quantitative dating has shown that formations pre-  
198 viously mapped as mid-to-late Miocene were deposited in the late Eocene (Gourbet et al.,  
199 2017). As well as the direct uncertainty as to when a sample was deposited, hotter global  
200 temperatures in the Eocene (Savin, 1977; Miller et al., 1987; Zachos et al., 2001) alter the  
201 relationship between isotopic composition and elevation, resulting in different paleoelevation  
202 estimates (filled and unfilled symbols in Figure 2b show paleoelevation estimates calculated  
203 using modern and Eocene relationships respectively). However, the differences in palaeoele-  
204 vation resulting from whether hotter temperatures are used are generally much less than the  
205 kilometre scale of interest for dynamic modelling, even for upper-bound estimates of Eocene  
206 temperature (region 4, Figure 2b, Hoke et al., 2014; Li et al., 2015; Tang et al., 2017; Wu  
207 et al., 2018).

208

209  $\delta^{18}O$  at sea level is also time-dependent. Licht et al. (2014) found very negative values  
210 of  $\delta^{18}O$  in an Eocene gastropod and rhinoceroid from Myanmar, taken as sea level refer-  
211 ences for the time. Preliminary results from isotopic analysis of soil-deposited carbonates in  
212 the same area show similarly low  $\delta^{18}O$  (Licht et al., 2019). A more negative starting value  
213 leads to lower palaeoelevation estimates, since Rayleigh fractionation predicts increasingly  
214 negative  $\delta^{18}O$  with elevation. These improved estimates of sea-level composition, as well as

215 the dating discussed above, have led to recalculations of palaeoelevation in south-east Tibet  
216 (Gourbet et al., 2017; Wu et al., 2018, shown as black symbols in Figure 2b-4, the original  
217 estimates are shown in gray), and we use these in our uplift rate calculations in preference  
218 to the original studies.

219

220 Uplift rates can be derived from stable-isotope palaeoaltimetry if samples can be taken  
221 from rocks of multiple ages at the same location or compared with the present-day elevation  
222 (blue dashed lines in Figure 2b). These rates, therefore, only reflect points in space and  
223 time which are preserved in the carbonate record. Where such rates can be inferred they are  
224 shown in Figure 2b. All but one of these inferred uplift rates are  $<0.3\text{mm yr}^{-1}$ .

225

226 In most of the regions shown in Figure 2, paleoelevations similar to present-day eleva-  
227 tions are found in the oldest sampled formations. To the north-west (region 1), Tang et al.  
228 (2017) suggest that topography may have been high since before the Eocene. Xiong et al.  
229 (2020) also found high topography in the Gonjo basin by the late Eocene, though their  
230 results suggest that this uplift may have occurred during the Eocene, giving possible early  
231 Eocene uplift rates of up to  $0.8\text{ mm yr}^{-1}$ , the only uplift rate  $>0.3\text{ mm yr}^{-1}$ . Although Xu  
232 et al. (2016)'s measurements have significant uncertainty in the moisture source, they sug-  
233 gest a lower bound for the elevation of the Longmen Shan in the late Miocene of  $\sim 3000\text{ m}$ ,  
234 compared to present-day elevations of  $2800\text{-}3700\text{ m}$ . To the south-east, region 5 may have  
235 experienced some uplift since the late Miocene, at rates  $<0.3\text{ mm yr}^{-1}$ , and region 6 was  
236 likely at its present elevation by the late Miocene.

237

238 These stable-isotope palaeoaltimetry results suggest that at least some areas of present-  
239 day south-east Tibet have been high since the late Eocene, and are likely to have reached  
240 present-day elevations prior to the onset of rapid exhumation inferred by Clark et al. (2005b)

241 from the incision of river gorges (gray region in Figure 2b). Uplift rates across south-east  
242 Tibet are likely to have been much lower ( $<0.3 \text{ mm yr}^{-1}$ ) than would be predicted if all the  
243 uplift in the region had occurred since the late Miocene. Recently published thermochronol-  
244 ogy is also consistent with this palaeoaltimetric data, suggesting that topography across the  
245 Longmenshan had begun to develop by the Oligocene (Wang et al., 2012), and that uplift  
246 may have been ongoing since the Paleocene (Liu-Zeng et al., 2018).

247

## 248 **3 Dynamical modelling**

249 In tandem with the palaeoaltimetry estimates summarised in section 2, we use numerical  
250 modelling to investigate the effect of lateral contrasts in lower crustal strength on the tem-  
251 poral evolution of mountain ranges. We first summarise the work of previous authors (sec-  
252 tion 3.1) and then describe the setup for the model used here (section 3.2) and our boundary  
253 conditions (section 3.3), before describing the model results in section 4. We emphasise that  
254 our model is intended to investigate the first-order effects of lateral strength contrasts on  
255 the multi-million-year development of long-wavelength topography in general, rather than  
256 to simulate the detailed evolution of south-east Tibet.

257

### 258 **3.1 Previous Models**

259 In regions of distributed deformation, the continental lithosphere can be modelled as a con-  
260 tinuum (commonly a viscous fluid), with motion driven by horizontal pressure gradients  
261 – resulting from gravity acting on elevation contrasts – and by the relative motion of the  
262 bounding plates (e.g. England and McKenzie, 1982, 1983; Houseman and England, 1986;  
263 Royden et al., 1997; Lamb, 2000; Flesch et al., 2001; Reynolds et al., 2015; Flesch et al.,

264 2018). Many authors use the thin-viscous-sheet model, which assumes negligible depth vari-  
265 ations in horizontal velocities (England and McKenzie, 1982, 1983). This model implicitly  
266 assumes that the top and base of the lithosphere experience shear tractions which are small  
267 in comparison to other components of the deviatoric stress tensor (here referred to as a stress-  
268 free boundary condition, after McKenzie et al., 2000). In the model, this corresponds to flow  
269 over a less viscous fluid (the asthenosphere). Such models can only produce steep-fronted  
270 topography if the lithosphere has an effective power-law rheology with a high stress exponent  
271 (typically greater than 3, i.e. shear-thinning, e.g. Houseman and England, 1986; Lechmann  
272 et al., 2011). The typical gradients in these models are still much less steep than those in  
273 steep-fronted mountain ranges such as the Himalayas and the Longmen Shan (England and  
274 Houseman, 1986). Geologically, stress exponents greater than 1 are associated with rocks  
275 deforming by dislocation creep (e.g. Stocker and Ashby, 1973).

276

277     Steep topographic gradients often occur adjacent to lateral contrasts in lithosphere strength.  
278 Such regions are commonly associated with large gradients in crustal thickness, and, if less  
279 viscous material flows over a higher viscosity region, this is equivalent to flow over a rigid  
280 base (defined as zero-horizontal velocity, or no-slip, after McKenzie et al., 2000). In such  
281 regions the thin-viscous sheet approximation breaks down, because flow over a rigid base is  
282 accommodated by vertical gradients of horizontal velocity in the flowing layer. Medvedev  
283 and Podladchikov (1999a) presented an extension to the thin-viscous sheet model to allow  
284 for rapid spatial variations in material properties, which was applied to 2D geodynamic  
285 scenarios by Medvedev and Podladchikov (1999b). An alternative approach is to use full  
286 thermo-mechanical models in either 2D (e.g. Beaumont et al., 2001) or 3D (e.g. Lechmann  
287 et al., 2011; Pusok and Kaus, 2015). Here we discuss a simplified approach, which allows us  
288 to incorporate flow over both stress-free and rigid boundaries into a single 3D model with a  
289 small number of adjustable parameters.

290

291 Previous studies incorporating vertical gradients of horizontal velocity have focused on  
292 reproducing geologically-instantaneous deformation in south-east Tibet (e.g. Copley, 2008;  
293 Lechmann et al., 2014; Bischoff and Flesch, 2019). These studies have demonstrated that key  
294 features of the instantaneous earthquake- and GPS-derived velocity field can be explained  
295 by lateral viscosity contrasts between cratonic blocks and the surrounding mountain ranges.  
296 Studies which have investigate the effects of these cratonic blocks on the temporal evolution  
297 of topography in south-east Tibet have used complex models at the scale of entire collision  
298 zones (e.g. Pusok and Kaus, 2015), or imposed external forcing or velocities to drive the  
299 flow (e.g. Cook and Royden, 2008). Here, we use a simple model of 3D crustal deformation,  
300 described below, to isolate the effects of lateral strength contrasts on the evolution of topog-  
301 raphy through time. Our interest is in understanding the physical controls on topographic  
302 evolution, in particular the development of laterally contrasting topographic gradients. Con-  
303 sideration of the temporal evolution of the topography is important because it allows us to  
304 investigate the constraints which can be provided by newly-available palaeoaltimetry data.

305

## 306 **3.2 Model Setup**

307 We model the lithosphere as a viscous fluid. The geometry and boundary conditions we  
308 use are based on the long-wavelength topography of south-east Tibet (Figure 3). Using a  
309 geometry similar to south-east Tibet allows us to make use of the palaeoaltimetric results  
310 described in Section 2 in assessing the uplift rates associated with the model.

311

312 GPS velocities (relative to Eurasia) in south-east Tibet are sub-parallel to topographic  
313 gradients (Figure 3). Movement of material along topographic gradients suggests that the  
314 deformation in south-east Tibet is influenced by gravitational potential energy contrasts.

315 The models we investigate here, therefore, include gravitational potential energy as a driv-  
316 ing force; deformation in these models is driven by gravity acting on crustal thickness con-  
317 trasts, without applied compressive forces or imposed boundary velocities. This category  
318 of models has been described by Lechmann et al. (2014) as “density driven”. Analogous  
319 models have been applied since the 1980s to the gravitational spreading of crustal thrust  
320 sheets (e.g. Ramberg, 1981; Merle and Guillier, 1989). Here we consider deformation on  
321 the lithosphere scale, rather than the lengthscale of individual thrust sheets. These studies  
322 also considered analogues between glaciological and geological gravity-driven deformation,  
323 including the possibility of both stress-free and no-slip basal boundary conditions (Ramberg,  
324 1981). We extend this analogy here by using methods from ice-sheet modelling to solve the  
325 governing equations.

326

327 We solve a simplified form of the Stokes’ equations using the method proposed by Pattyn  
328 (2003), which includes vertical gradients of horizontal velocities. This method allows us to  
329 model flow over a stress-free base and also a rigid base, representing regions of strong lower  
330 crust, unlike the original thin-viscous-sheet model (England and McKenzie, 1982, 1983). The  
331 implementation and more mathematical details of this approach are given in Appendix A.

332

333 The method we use here has previously been used to calculate instantaneous strain rates  
334 in south-east Tibet (Copley, 2008). Reynolds et al. (2015) extended this approach to model  
335 the temporal evolution of the Sulaiman Ranges by re-writing the incompressibility condi-  
336 tion as a diffusion equation for topography (Pattyn, 2003). We use an improved method  
337 (Appendix A) to solve this diffusion equation, calculating diffusivities on a staggered grid,  
338 and using the generalised minimum residual method (Saad and Schultz, 1986) to solve the  
339 resulting sparse matrix equations. We use a regular horizontal grid of 15 km×15 km, and  
340 20 grid points in the vertical, which are re-scaled at each time step (Appendix A; Pattyn,

341 2003). The assumptions and set-up of this model are discussed below.

342

343 We model the deforming crust as an isoviscous, Newtonian fluid. Using a simple rheology  
344 allows us to test the extent to which topographic evolution in south-east Tibet is controlled  
345 by the presence of lateral lower crustal strength contrasts, and whether additional rheological  
346 complexity is required to explain the geophysical and geological observations. The simple  
347 rheology we use contrasts with the approach of previous authors studying the effect of a  
348 strong craton on the evolution of topography in south-east Tibet. For example, Chen et al.  
349 (2013a) used a 2D model with multiple rock types and an assumed geotherm. Cook and  
350 Royden (2008) included a weak lower crustal channel and drove deformation within their  
351 model through an imposed velocity at its base. By using a simpler rheology, we are able  
352 to isolate the effects of lower crustal strength contrasts on the evolution of topography. We  
353 discuss the possible effects of a more complicated rheology in Section 5. The equations re-  
354 lating velocities in the fluid to gradients in topography are linearly dependent on the fluid  
355 viscosity (Appendix A) so although we use a viscosity of  $10^{22}$  Pas here (as suggested for  
356 south-east Tibet by Copley and McKenzie, 2007), we expect that these models will apply to  
357 different viscosities with scaled times and velocities. For example, we expect the topography  
358 after 50 Myr of model evolution with a viscosity of  $10^{22}$  Pas to be the same as that after  
359 5 Myr for a viscosity of  $10^{21}$  Pas. The velocities would be 10 times greater in the  $10^{21}$  Pas case.

360

361 We impose Airy isostatic compensation at the base of the crust, relative to a column of  
362 mantle (Flesch et al., 2001), with densities of  $2700 \text{ kg m}^{-3}$  and  $3300 \text{ kg m}^{-3}$  respectively.  
363 Assuming isostatic compensation neglects flexural support of the topography. By using a  
364 viscous model, we are implicitly considering long-wavelength deformation (motivated by the  
365 long-wavelength shape of the topography in Figure 3). Free-air gravity anomalies from south-  
366 east Tibet (Fielding and McKenzie, 2012) suggest that flexure plays a role in supporting the



367 topography on relatively short-wavelengths ( $\sim 50$  km into the Longmen Shan), which means  
368 that isostatic compensation is an appropriate assumption throughout most of the model  
369 domain. At the edge of the basin region, where flexural support may be important, flex-  
370 ure would be expected to give a shape for the basal boundary that is intermediate between  
371 full isostatic compensation, which we use here, and a base which cannot move vertically in  
372 response to loading, a case which is often considered in the fluid dynamics literature (e.g.  
373 Huppert, 1982). The implications of assuming isostatic compensation are discussed in Sec-  
374 tion 4.

375

376 Figure 4 shows a diagram of our model setup. High viscosity regions, analogous to the  
377 strong lower crust of the Sichuan Basin and the Central Lowlands of Myanmar, are simu-  
378 lated by setting horizontal velocities to zero in part of the model with a specified thickness  
379 (“basal thickness”, grey areas in Figure 4). Flow can occur over and around these rigid  
380 regions (“basins”, Basin E and Basin W in Figure 4). The basal thickness is equivalent to  
381 the thickness of strong lower crust. The Sichuan Basin is connected to the South China  
382 craton (e.g. Li and Van Der Hilst, 2010), which provides a resistive force, so the basins  
383 in our model are not advected with the flow. By setting velocities to zero in these basin  
384 regions, we are assuming that the lower crust in the Sichuan Basin and Central Lowlands  
385 of Myanmar has behaved rigidly over the 50 Myr of deformation which we model. This  
386 approach is suggested by inferences of strong lower crust and upper mantle in the Sichuan  
387 Basin and Central Lowlands of Myanmar (Section 1; Li and Van Der Hilst, 2010; Huang  
388 et al., 2014). The lower crustal viscosity required for our assumption of rigidity to hold can  
389 be calculated from the gravitational potential energy contrast between the Longmen Shan  
390 and Sichuan Basin. The crustal thicknesses in the Longmen Shan and Sichuan Basina are  
391 65 and 36–40 km respectively (e.g. Liu et al., 2014), with 4.5 km of elevation contrast. We  
392 assume a constant crustal density,  $\rho_c = 2700 \text{ kg m}^{-3}$ . The horizontal driving force associ-

ated with this gravitational potential energy contrast can be calculated by integrating the  
pressure difference between the two columns of crust (e.g. Artyushkov, 1973; Molnar and  
Tapponnier, 1978; Dalmayrac and Molnar, 1981; Molnar and Lyon-Caen, 1988), giving a  
maximum horizontal driving force of  $7 \times 10^{12} \text{ N m}^{-1}$ , similar to that applied by Tibet on  
cratonic India (e.g. Copley et al., 2010). Assuming that this force is distributed uniformly  
with depth in the crust, this horizontal driving force results in a maximum deviatoric normal  
stress acting on the Sichuan Basin of  $\sim 120 \text{ MPa}$ . This stress, and therefore the required vis-  
cosity, would be lower if any of the stress were supported by the mantle. If this topographic  
contrast has existed since 50 Mya (the effective start time of our model) then for the Sichuan  
Basin, which is  $\sim 300 \text{ km}$  wide, to have deformed by less than one grid cell in our model  
( $15 \text{ km}$ ), requires a strain rate in the lower crust less than  $3.2 \times 10^{-17} \text{ s}^{-1}$ . In this scenario  
the viscosity of the crust in the Sichuan Basin would need to be greater than  $\sim 4 \times 10^{24} \text{ Pas}$   
to remain undeformed by horizontal forces associated with gravitational potential energy  
contrasts. The viscosity required would be lower if the topographic contrast were supported  
for a shorter time. We can test whether this viscosity is reasonable using laboratory-derived  
flow laws. We use the dry flow laws for typical lower crustal minerals from Bystricky and  
Mackwell (2001) and Rybacki et al. (2006), and calculate the temperature corresponding to  
a viscosity of  $4 \times 10^{24} \text{ Pas}$  at the Moho ( $36\text{--}40 \text{ km}$  Liu et al., 2014), assuming lithostatic  
pressure and a grain size of  $1 \text{ mm}$ . For both flow laws, the viscosity will be  $\geq 4 \times 10^{24} \text{ Pas}$  if  
the temperature is less than  $\sim 800\text{--}900^\circ\text{C}$ . Moho temperatures in undefining Precambrian  
crust are typically  $\sim 600^\circ\text{C}$  (McKenzie et al., 2005), meaning that the viscosity required  
for the Sichuan Basin to behave rigidly on the timescales of our model is consistent with  
laboratory-derived flows laws. Rather than adding an additional parameter to our model  
we therefore model the basin lower crust as rigid. As discussed in section 1, the geological  
structure of the Central Myanmar Basin is less well constrained than that of the Sichuan  
Basin, but it also acts in a rigid manner, so for simplicity we make the same assumption there.

419

420 Outside the basins, the base of the current in our models is stress-free (vertical derivatives  
421 of horizontal velocities are zero; England and McKenzie, 1982, 1983; Copley and McKenzie,  
422 2007), implying that the asthenosphere imposes negligible shear stress on the base of the  
423 lithosphere. Since we only model the deformation of the crust, we are assuming that the crust  
424 and lithospheric mantle deform coherently in the region with the stress-free base, and that  
425 shearing over the lithospheric mantle plays a limited role in the force balance of the lower  
426 crust. For this assumption to hold true, the lithospheric mantle should have a sufficiently  
427 low viscosity that dominant stress driving its motion is the deviatoric stress resulting from  
428 flow in the lower crust, rather than the stress imposed on vertical planes by shearing past the  
429 basins. From our modelling, the deviatoric strain rate in the centre of the inter-basin region  
430 is  $\sim 5 \times 10^{-16} \text{s}^{-1}$ , giving a deviatoric stress of 10 MPa in the lower crust, using a crustal  
431 viscosity of  $10^{22}$  Pas. The shear strain rate on the basin margins is  $\sim 3 \times 10^{-15} \text{s}^{-1}$ . For our  
432 assumption to hold, therefore, the viscosity of the lithospheric mantle should be  $\ll 10^{21}$  Pas.  
433 Using the flow laws derived for wet olivine by Hirth and Kohlstedt (2003) with a grain size  
434 of 1 mm, 1.5GPa pressure (lithostatic pressure at the Moho beneath  $\sim 55$  km thick crust),  
435 1 GPa water fugacity, and a strain rate of  $10^{-16} \text{s}^{-1}$ , effective viscosities less than  $10^{21}$  Pas  
436 correspond to temperatures above  $\sim 400\text{--}700^\circ\text{C}$  (depending on whether deformation occurs  
437 by dislocation or diffusion creep). Effective viscosities less than  $10^{19}$  Pas (i.e. such that  
438 the shear stress imposed on the lithospheric mantle at the basin margins would be two or-  
439 ders of magnitude less than the driving deviatoric stress in the lower crust) correspond to  
440 temperatures above  $\sim 800^\circ\text{C}$ . These temperatures are consistent with temperature estimates  
441 from lithospheric mantle xenoliths in south-east Tibet (Yu et al., 2010; Liu et al., 2013),  
442 suggesting that modelling crustal deformation with a stress-free base outside the basin re-  
443 gions is reasonable. Copley (2008) also demonstrated the possibility of coherent lower crust  
444 and lithospheric mantle deformation in south-east Tibet using rheologies extrapolated from

445 laboratory flow laws. Although such extrapolations lead to vertical gradients in viscosity, in  
446 many cases these gradients, and the length-scales over which they occur, are insufficient to  
447 result in appreciable contrasts in horizontal velocities.

448

449 The top surface of the current in our models is stress-free throughout the model domain,  
450 representing the lack of significant tractions imposed by the atmosphere. We track particles  
451 on this surface, which move with the horizontal velocity at their location at each time step.  
452 These particles are analogous to the samples used in palaeoaltimetric studies.

453

454 In some models we investigate the interaction between erosion and propagation of the  
455 current by incorporating an erosive term;

$$\frac{\partial s}{\partial t} = -\kappa |\nabla s|, \quad (1)$$

456 where  $\kappa$  is a constant. Gradient-dependent erosion is suggested by higher erosion rates and  
457 greater cumulative erosion in the Longmen Shan than in the interior of the Sichuan Basin  
458 and Tibetan Plateau (Richardson et al., 2008). This erosive term has the same derivation as  
459 the classic Culling model (Culling, 1960), but assumes that eroded material is removed from  
460 the model domain. This assumption is consistent with Hubbard et al.'s (2010) proposal that  
461 sediment is transported away from the Sichuan basin by the Yangtze River.

462

### 463 **3.3 Lateral Boundary Conditions**

464 The mathematical details of the boundary conditions used in our model are given in Ap-  
465 pendix A. Here we summarise these boundary conditions and explain their physical motiva-  
466 tion.

467

468 Initially ( $t = 0$ ), the domain is filled with a 40 km-thick layer of fluid ( $H_0$ , Figure 4),  
469 chosen to represent generic, undeformed continental crust. There may have been pre-existing  
470 topography in south-east Tibet before the onset of Cenozoic deformation (Burchfiel et al.,  
471 1995; Hubbard et al., 2010). However, the shape of this topography is poorly constrained,  
472 so we assume an initially flat, uniform layer for simplicity.

473

474 At one edge of the model domain ( $y = 0$ ) fluid flows into the region, analogous to the lat-  
475 eral growth of a mountain range, in this case from central Tibet into south-east Tibet. The  
476 topography along this boundary is 4.5 km above the surface of the 40 km thick layer in the  
477 remainder of the model domain, similar to the mean elevation of the Tibetan Plateau above  
478 the Sichuan Basin (Figure 1). This height is kept constant throughout the model evolution.  
479 Using a fixed-height boundary condition is analogous to assuming that the central Tibetan  
480 plateau has been at its present elevation throughout the development of high topography in  
481 south-east Tibet. This simple assumption allows us to isolate the effects of lateral variations  
482 in lower-crustal strength in south-east Tibet, and is consistent with palaeoaltimetric data,  
483 which suggest that the central plateau has been high since at least the Eocene (e.g. Rowley  
484 and Currie, 2006). The velocity perpendicular to the influx ( $y = 0$ ) boundary is set by the  
485 horizontal driving force associated with an undeforming reservoir of high material (i.e. the  
486 central Tibetan Plateau), which can supply fluid to the current at the same rate at which  
487 fluid moves away from the boundary (Figure 4, Appendix A; Reynolds et al., 2015). We set  
488 the velocity parallel to this boundary to zero ( $u = 0$  on  $y = 0$ ), motivated by the small ve-  
489 locity component parallel to the NW boundary of Figure 3. The starting topography within  
490 the model domain adjacent to this influx boundary has a constant slope in the  $y$  direction  
491 (Figure 4); its gradient does not affect the model results after the first few timesteps.

492

493 At the right-hand end of the domain as shown in Figure 4 ( $y = y_{max}$ ), and beyond the  
494 basins ( $y > y_b$ ), we assume that there is an external reservoir of undeformed, 40 km thick  
495 crust, which determines the boundary-perpendicular velocities. We assume that the hori-  
496 zontal driving force associated with this 40 km-thick crust (e.g. Artyushkov, 1973; Molnar  
497 and Tapponnier, 1978; Dalmayrac and Molnar, 1981; Turcotte and Schubert, 2014) acts per-  
498 pendicular to the boundary, rather than anti-parallel to the maximum topographic gradient.  
499 This assumption is equivalent to the maximum topographic gradient being perpendicular  
500 to the boundary. We find that this assumption has little effect on the modelling results,  
501 and makes the calculations much less computationally expensive because we do not need  
502 to iterate over the velocity calculation at each timestep. However, making this assumption  
503 does mean that we require a second condition for the boundary-parallel velocity. We set  
504 the derivatives of boundary-parallel velocities perpendicular to these boundaries to zero (i.e.  
505  $\frac{\partial u}{\partial y} = 0$  on  $y = y_{max}$ , and  $\frac{\partial v}{\partial x} = 0$  on  $x = 0$  and  $x = x_{max}$ ). This second condition is equiv-  
506 alent to assuming that the crust outside the model domain does not exert significant shear  
507 stresses on the domain boundary. These boundary conditions are consistent with the lack of  
508 significant faulting, low earthquake- and GPS-derived strain rates, and uniform,  $\sim 35$ – $40$  km  
509 crustal thicknesses (Xu et al., 2013) outside the region of south-east Tibet which corresponds  
510 to our model domain (Figure 3).

511

512 Along  $x = 0$  and  $x = x_{max}$  we use a reflection boundary condition up to the end of the  
513 basins ( $y < y_b$ ). This is equivalent to assuming that mountains also exist to either side of  
514 the model domain, and are behaving in the same manner in these regions; analogous to high  
515 topography existing to the north of the Sichuan Basin and the Central Lowlands of Myanmar.

516

## 4 Results & Comparison to South East Tibet

We initially use symmetric models (i.e. where the two basins with strong lower crust have the same size and are the same distance from the influx boundary) to investigate the effects of changing basal thickness and inter-basin width (defined in Figure 4) on the evolution of topography. Figure 5 shows the results of a model with symmetric basins of radius 450 km (grey semi-circles, Figure 5c, equivalent to an inter-basin width of 600 km), and basal thickness 15 km. Times referred to are since the start of the model and elevations are given relative to the surface of 40 km-thick, isostatically-compensated crust. As discussed in Section 3, the velocity and, therefore, the rate of topographic evolution, are expected to scale linearly with the viscosity. We therefore expect that the topography after 50 Myr of model evolution with a viscosity of  $10^{22}$  Pas (as shown in Figure 5a) would correspond to that after 5 Myr for a viscosity of  $10^{21}$  Pas.

Regions with a stress-free base develop gentle topographic gradients. Deformation in these regions is effectively by pure shear of vertical planes; gentle topographic gradients result from the quasi-depth-independent horizontal velocities. Gentle topographic gradients are also a feature of thin-viscous-sheet models (England and McKenzie, 1982, 1983, even where these models use high stress-exponents; Section 3.1), which have the same, stress-free, basal boundary condition. The topographic gradients in the stress-free regions are very similar in magnitude to the south-eastwards topographic gradients in the high region between the Sichuan Basin and the Central Lowlands of Myanmar (compare Figures 6h and 6f – the topographic profile location is shown in Figure 2a). We expect these gradients to be partially controlled by the location of the model boundaries which, as discussed in Section 3.3 are consistent with the deformation and crustal thicknesses in south-east Tibet.

542 In contrast to regions with a stress-free base, steep topographic gradients develop in the  
543 basin regions, suggesting that steep topography can form as a result of mountain ranges  
544 overriding rigid lower crust. Although in the inter-basin region the specific gradients, and  
545 the slow propagation of topography in the  $y$ -direction (Figures 6b, d and f) are partially  
546 controlled by the location of the model boundaries, we apply the same boundary conditions  
547 along the whole length of  $y = 0$  and  $y = y_{max}$ . The development of very different topo-  
548 graphic gradients in regions with and without a rigid base (compare Figures 6a, c and e  
549 to Figures 6b, d and f) therefore, shows the first-order control exerted by the basin regions  
550 on the shape of the topography. These different topographic gradients are consistent with  
551 previous work showing that flow over a rigid base results in steeper gradients than flow over  
552 a stress-free base (e.g. McKenzie et al., 2000).

553

554 The topography also propagates more slowly in the basin regions than in the region be-  
555 tween them (compare Figure 6 c and d). Where flow occurs over a rigid base, the velocity  
556 depends on the square of the flow depth (Huppert, 1982). Increasing the basal thickness  
557 (analogous to having a thicker rigid lower crust or a thinner overlying layer of deformable  
558 rock) therefore, reduces the distance which the current propagates into the basin in a given  
559 time, and also results in steeper topographic profiles where the flow overrides the basin.  
560 This effect is demonstrated by Figure 6, which shows profiles through models with the same  
561 basin locations as in Figure 5, but with varying basal thicknesses. The locations of these  
562 profiles are shown in Figure 5b. The lateral extent of the region which has a rigid base is  
563 shown by grey bars on the profiles. Figures 6 a & b, c & d and e & f have basal thicknesses  
564 of 0 km (only the base is rigid), 15 km and 30 km respectively. A proportionally thicker  
565 rigid region (e.g. Figure 6e) means that the current is flowing into a thinner fluid layer,  
566 so tends to develop a sharper nose, as shown by McKenzie et al. (2000). The topographic  
567 gradients across the Longmen Shan (Figures 6g) are very similar to those in our model for



568 a basal thickness of 30 km (corresponding to 10 km initial thickness of deformable rock in  
569 the basin regions). This basal thickness is consistent with  $\sim 10$  km of sediment overlying  
570 Paleoproterozoic basement in the Sichuan Basin (Hubbard and Shaw, 2009).

571

572 Erosion also leads to steeper topographic gradients, and hinders current propagation in  
573 the basins. The dashed lines in Figure 6c and d show the results of eroding the topography  
574 with  $\kappa = 4 \text{ mm yr}^{-1}$  in equation (1). The erosive term we use is proportional to gradient  
575 (Section 3), meaning that the steep slopes in the basins are affected more than gentle slopes  
576 in the inter-basin region (compare dashed lines in Figures 6c and d). With  $\kappa = 4 \text{ mm yr}^{-1}$  the  
577 topography is quasi-stationary on the basin margins between 15 and 50 Myr (dashed blue  
578 and red lines in Figure 6c), demonstrating that erosion can stop the propagation of topog-  
579 raphy in these regions (as suggested by Koons, 1989, for the South Island of New Zealand),  
580 but not in the region of fast flow between the basins. The similar position of the present-day  
581 Longmen Shan and the Paleogene deformation front adjacent to the Sichuan Basin (derived  
582 from stratigraphic thicknesses of foreland basin sediments; Richardson et al., 2008) could,  
583 therefore, result from erosion acting on topography which would otherwise be propagating  
584 over the basin. Such an effect is possible because of the slow propagation of topography over  
585 rigid lower crust.

586

587 The distance between basins controls the velocity of the current in the region between  
588 them. Figure 7 shows the topographic and velocity profiles resulting from different inter-  
589 basin widths, with constant basal thickness (15 km). Greater inter-basin widths result in  
590 faster velocities perpendicular to the profile ( $v$ , Figures 7b, d, f). Flow in the inter-basin  
591 region is dominated by simple shear of horizontal planes – similar to that between two rigid  
592 walls (as suggested by Copley and McKenzie, 2007), with maximum velocity proportional to  
593 width squared. The width of the rapidly deforming region between the Sichuan Basin and

594 the Central Lowlands of Myanmar is  $\sim 500$  km. Observed GPS velocities relative to Eurasia  
595 in the centre of this region are  $\sim 20$  mm yr<sup>-1</sup>. Inter-basin velocities in our model are similar  
596 to these GPS velocities for an inter-basin width of 600 km, which suggests that the viscosity  
597 we use for our modelling ( $10^{22}$  Pas) is reasonable.

598

599 As discussed in section 3.2, our models do not include flexural support of the topogra-  
600 phy. If we did include flexural support we would not expect to see qualitatively different  
601 topography, because the wavelengths associated with such support are small in compari-  
602 son to the scale of our model. Viscous models of the crust, such as the one we use here,  
603 implicitly investigate long wavelength deformation, at scales longer than individual faults  
604 (Figure 3, England and McKenzie, 1982, 1983). Gravity anomalies demonstrate flexural ef-  
605 fects in south-east Tibet acting on wavelengths less than  $\sim 50$  km (Fielding and McKenzie,  
606 2012), and isostatic compensation throughout the region of high topography (Jordan and  
607 Watts, 2005; Fielding and McKenzie, 2012). Fielding and McKenzie (2012) found a lower  
608 bound on the elastic thickness of the Sichuan Basin of 10 km (although this value is poorly  
609 constrained since the basin is too small for the full flexural wavelength to be measured) and  
610 an elastic thickness of 7 km for the adjacent high topography. Flexure may provide local  
611 support to the topography where it overthrusts the Sichuan Basin (in our model, over the  
612 horizontally rigid basin). The topographic gradient in this region of our model, therefore,  
613 represents an end-member in which the rigid (zero horizontal velocity) base is free to move  
614 vertically. The other end-member, in which the base cannot move vertically in response to  
615 being loaded, also leads to steep fronts (Huppert, 1982), even when flow is into a layer which  
616 is much thicker than the topography (McKenzie et al., 2000). The rigid nature of the basal  
617 boundary (i.e. the no-slip condition on the base of the fluid) controls the shape of the topog-  
618 raphy, rather than whether or not this boundary is able to deform vertically (McKenzie et al.,  
619 2000). Ball et al. (2019) demonstrated that flexural effects are primarily important near the

620 nose of a viscous current, but that such currents over a flexed base can still form steep  
621 topographic gradients provided the base of the current has a no-slip boundary condition.  
622 The difference in basal boundaries conditions, and the depth of deformable rock, therefore,  
623 provide a first-order explanation for contrasting topographic gradients in south-east Tibet,  
624 even if our models do not capture the precise, short-wavelength details of the topography.

625

626 The elevation histories of particles we track at the surface of the current (Figure 5d) show  
627 that uplift rates from our model are  $\sim 0.1\text{--}0.5\text{ mm yr}^{-1}$  in the centre of the inter-basin region  
628 (red star in Figure 5d), similar to the  $< 0.3\text{ mm yr}^{-1}$  uplift rates derived from palaeoal-  
629 timetry (Section 2, Figure 2). The highest uplift rates in our model ( $\sim 0.5\text{ mm yr}^{-1}$ , green  
630 diamond) occur within the first 10–15 Myr of model evolution for particles moving into the  
631 inter-basin region. These rates and locations are similar to those in the only region (region  
632 1, the Gonjo basin, Figure 2) where uplift rates  $> 0.3\text{ mm yr}^{-1}$  have been suggested from  
633 palaeoaltimetry in South East Tibet. However, our modelling also demonstrates that the  
634 interpretation of palaeoelevation results is not straightforward. Figure 5 shows that ma-  
635 terial at the surface may be transported long distances (hundreds of kilometres over tens  
636 of millions of years for the viscosity used here). The advection of particles with the flow  
637 means that elevation histories may be complex, with particle elevations decreasing “south”  
638 (towards  $y = y_{max}$ ) of the inter-basin region as the current spreads laterally (the same effect  
639 which leads to the extensional strain rates described below). Pedogenic carbonates which  
640 are found to have been high in the late Eocene–early Miocene (Hoke et al., 2014; Li et al.,  
641 2015; Gourbet et al., 2017) could have been deposited at similar latitudes to samples from  
642 the Longmen Shan, which were at their present elevation in the late Miocene (Xu et al., 2016).

643

644 By considering the principal axes of the horizontal the strain-rate tensor at the surface  
645 of our model (Figure 5b) as analogous to the strain rate in the brittle crust (Houseman

646 and England, 1986), we can draw comparisons between our model and the geodetic- and  
647 seismic-strain rates in south-east Tibet. The largest strain-rates in both our model and in  
648 south-east Tibet are associated with shear at the basin margins. Strain rates equivalent to  
649 left-lateral shear adjacent to Basin E (Figure 4), and right-lateral shear adjacent to Basin  
650 W (Figure 4) are analogous to left-lateral slip on the Xianshuihe Fault and right-lateral slip  
651 on the Nuijiang and Sagaing Faults (and adjacent right-lateral faults) respectively.

652

653 Compressive strain rates associated with steep topography at the edges of the basins are  
654 small in comparison to these shear strain rates. In the context of south-east Tibet, this  
655 suggests that the steep topography and low shortening rates across the Longmen Shan could  
656 result from flow of weaker material over the rigid lower crust of the Sichuan Basin (Copley  
657 and McKenzie, 2007; Copley, 2008; Fielding and McKenzie, 2012), without a low-viscosity,  
658 lower-crustal channel.

659

660 The principal axes of the horizontal strain-rate tensor at the surface of our models show  
661 two extension-dominated regions (red ellipses in Figure 5b), with similar locations and ori-  
662 entations to the normal faulting in south-east Tibet (red ellipses and focal mechanisms in  
663 Figure 1b). The extensional strain rates in these parts of our model are  $\sim 2$ – $5$  times larger  
664 than the compressional strain rates, so these regions are equivalent to mixed strike-slip and  
665 normal faulting, with normal faulting dominating. Extension in the y direction ‘north’ of  
666 the basins (top white ellipse in Figure 5b) is comparable to the northern group of normal  
667 faults in Figure 1, which strike perpendicular to both topographic gradient (accommodat-  
668 ing extension parallel to the topographic gradient) and GPS velocities relative to Eurasia  
669 (Figure 3). Our modelling suggests that this extension may result from a velocity increase  
670 where the topography flows through the inter-basin region. The second region of extension  
671 occurs where fluid spreads out laterally to the ‘south’ of the basins; increasing the surface

672 area of the current. This extension perpendicular to topographic gradients is shown by the  
673 bottom white ellipse in Figure 5b. The southern group of normal faults shown in Figure 1  
674 also accommodate extension perpendicular to the topographic gradients.

675

676 Figure 8 shows the results of changing the shape of one of the basins to be more similar  
677 to that of the Central Lowlands of Myanmar. The region of shear which develops adja-  
678 cent to this basin is broader than that adjacent to a semi-circular basin because the flow  
679 is approximately parallel to the change in basal boundary condition, resulting in greater  
680 horizontal tractions on vertical planes. This broader region of shear is similar to the area of  
681 distributed left-lateral faulting east of the Sagaing fault (Figure 1a), which accommodates  
682 right-lateral shear through vertical-axis rotations (Copley, 2008). The lateral extent of this  
683 shear in south-east Tibet may, therefore, be controlled by the geometry of the rigid lower  
684 crust in the Central Lowlands of Myanmar.

685

## 686 **5 Discussion**

687 Our model, considering the effect of lateral lower crustal strength variations consistent with  
688 geophysical and geological observations, allows us to reproduce the main features of the  
689 present-day topography, strain-rate and velocity field in south-east Tibet, and uplift rates  
690 from palaeoaltimetry. These results demonstrate that lateral strength contrasts, in the form  
691 of regions of rigid lower crust, provide a first-order control on the temporal evolution of  
692 mountain ranges (Figure 9). Below we discuss our key findings and their application to  
693 mountain ranges in general.

694

695 In our model, which has mechanically-coupled upper and lower crust, surface uplift rates

696 are  $< \sim 0.5 \text{ mm yr}^{-1}$ . These gradual uplift rates are consistent with palaeoaltimetry results  
697 in south-east Tibet, suggesting that no low-viscosity, lower-crustal channel is required to  
698 explain the evolution of topography in this region. However, the results of particle track-  
699 ing show that material at the surface where the crust flows over a stress-free base may be  
700 transported long distances (hundreds of kilometres over millions of years for the viscosity  
701 used here, consistent with fault offsets reported over shorter time periods, Wang and Burch-  
702 fiel, 1997). Calculated palaeoelevations, therefore, estimate the palaeoelevation of the place  
703 where the sample was deposited, rather than the palaeoelevation of its present-day location.  
704 Accounting for this lateral transport is also important for converting the oxygen-isotope  
705 composition of carbonates to palaeoelevation, potentially requiring greater continentality  
706 corrections. Although strike-slip faults do not build mountains, they can move them hori-  
707 zontally for large distances.

708

709 Our modelling demonstrates that differences in basal boundary condition, analogous to  
710 the presence or absence of strong lower crust, can lead to the development of contrasting  
711 topographic gradients. In particular, steep gradients arise naturally from flow over a rigid  
712 (no-slip) base. The present-day compressional strain rates across these steep margins are  
713 low in comparison to the rates of shear where deformation is parallel to the basin margins,  
714 in both our model and in south-east Tibet (Shen et al., 2005; Zheng et al., 2017). This  
715 combination, of steep-fronted topography and low compressional strain rates, is a feature  
716 of other parts of the India-Eurasia collision. Steep topographic gradients on the northern  
717 margin of the Tibetan Plateau, adjacent to the Tarim basin ( $\sim 3 \text{ km}$  over  $50 \text{ km}$ ), and the  
718 low rate of shortening ( $0\text{--}3 \text{ mm yr}^{-1}$ , e.g. Zheng et al., 2017) across the basin margin, are  
719 similar to those in the Longmen Shan. Increasing Moho depths from north to south across  
720 the margin (Wittlinger et al., 2004), and the flexural signal seen in free-air gravity anoma-  
721 lies (e.g. McKenzie et al., 2019), suggests that the western edge of the Tarim Basin may

722 underthrust the western Kunlun ranges, which would provide a rigid base to the flow of  
723 crustal material from northern Tibet, in a similar manner to the Sichuan Basin in south-east  
724 Tibet. The temporal evolution of topography adjacent to the Tarim Basin may, therefore,  
725 also be controlled by the lateral strength contrast between rigid lower crust in the Tarim  
726 Basin and lower viscosity crust in Tibet. The motion of southern Tibet over rigid India is  
727 likely to represent the same effect. However, the rates of motion in southern Tibet are more  
728 rapid than in northern Tibet, perhaps due to differences in the thicknesses, temperatures or  
729 compositions of the crust in India and the Tarim basin (McKenzie et al., 2019).

730

731 More generally, the control on topographic evolution provided by lateral strength con-  
732 trasts, particularly the low rates of propagation of topography into regions with rigid lower  
733 crust (Figures 6, 9), suggests an explanation for the correlation of cratonic regions with steep  
734 edges of mountain belts (including the Atlas mountains, the Caucasus and older orogenies  
735 such as the Appalachians and Rockies in North America) noted by McKenzie and Priestley  
736 (2008). Cratonic regions are likely to have relatively strong lower crust (e.g. Jackson et al.,  
737 2008), so our results suggest that the propagation of topography into these regions will be  
738 slow in comparison to adjacent regions where the lower crust has lower viscosity.

739

740 We also find that the thickness of strong lower crust, and of deformable material (such as  
741 sediments) above it, controls the extent of mountain range propagation and the morphology  
742 of the range front. Larger thicknesses of deformable rock (fluid layer above the rigid base  
743 in our models) lead to more rapid propagation of topography over regions with strong lower  
744 crust, and to shallower topographic gradients. This result is likely to apply to mountain  
745 ranges globally. The occurrence of thin-skinned deformation of sediments above the edge of  
746 the South American craton, in the foothills of the Eastern Cordillera of the Andes (Lamb,  
747 2000), suggests that the deformation in this region is comparable to flow over a rigid base.

748 The foothills in the southern Bolivian Andes extend further east than those in the north, and  
749 have lower topographic gradients. This broader foothill region correlates with higher sedi-  
750 ment thicknesses in the bounding basin (McGroder et al., 2014), similar to the current in our  
751 model propagating further over a rigid base where the deformable layer is thicker (Figure 6c  
752 and e). Wimpenny et al. (2018) suggested that this effect might lead to the onset of extension  
753 in the adjacent mountains. Along-strike variations in sediment thickness can also explain  
754 variations in the morphology of the Indo-Burman Ranges (Ball et al., 2019), although there  
755 mountain building is driven by the subducting plate, which advects sediment laterally, as  
756 well as by contrasts in gravitational potential energy. Ball et al. (2019) highlighted that it is  
757 the thickness of deformable sediment, rather than the total sediment thickness, which is im-  
758 portant in controlling morphology. Although beyond the scope of this study, we expect that  
759 along-strike variations in the viscosity of the deformable rock, as well as its thickness, could  
760 lead to similar changes in morphology. In the Zagros mountains, for example, along-strike  
761 variations in the width of high topography could potentially correlate with the presence or  
762 absence of weak salt layers (Nissen et al., 2011). Similarly, the prominent curvature of the  
763 Sulaiman Ranges, and their projection beyond the general  $\sim$ north–south strike of the Pak-  
764 istan range front, has been proposed to result from a weaker package of sediments beneath  
765 them (Reynolds et al., 2015).

766

767 For crust in south-east Tibet, it is not clear whether ductile deformation is dominated  
768 by diffusion creep, which is Newtonian with a stress exponent of 1, or dislocation creep,  
769 which has a power-law rheology with a stress exponent greater than 1, (e.g. Stocker and  
770 Ashby, 1973). In our modelling, we have, therefore, taken the simplest approach, which  
771 is to use a Newtonian rheology with a constant viscosity. Our models show that such a  
772 rheology can produce steep topographic gradients where flow occurs over a rigid base, such  
773 as strong lower crust. In contrast, in models where depth variations in horizontal velocity



774 are neglected, steep topographic gradients require a power-law rheology with a high stress  
775 exponent, and, even then, these gradients are much shallower than those in the Longmen  
776 Shan (Section 3.1, Houseman and England, 1986; England and Houseman, 1986; Lechmann  
777 et al., 2011). If dislocation creep does control ductile deformation, the vertically-integrated  
778 strength of the lithosphere can be represented as a single power-law rheology (Sonder and  
779 England, 1986). An interesting question, therefore, is whether the steep topographic gradi-  
780 ents in our model would still form if we had used a power-law, rather than a Newtonian,  
781 rheology. A higher stress-exponent would tend to localise deformation in regions of high  
782 strain rate, such as immediately above the rigid lower crust in the basin regions. The second  
783 invariant of the strain rate tensor in these regions of our model is  $\sim 10^{-15} \text{ s}^{-1}$ , consistent with  
784 geodetically- and geologically-estimated strain rates in tectonically active regions (Fagereng  
785 and Biggs, 2019). For a viscosity of  $10^{22} \text{ Pas}$  this strain rate corresponds to a stress of  
786  $\sim 10 \text{ MPa}$ , typical of earthquake stress drops (Kanamori and Anderson, 1975; Allmann and  
787 Shearer, 2009). If the crust were to deform with a power-law rheology with a stress-exponent  
788 of 3, and assuming a strain rate in the rest of the model domain of  $\sim 10^{-16} \text{ s}^{-1}$ , these strain  
789 rates would lead to a local drop in viscosity from  $10^{22} \text{ Pas}$  to  $\sim 2 \times 10^{21} \text{ Pas}$ , which might  
790 lubricate the base of the current. However, the flow over the rigid base would still be much  
791 slower than that with a stress-free base, and have a non-linear dependence on the thickness  
792 of the current, meaning that we would still expect contrasting topographic gradients to de-  
793 velop. Mathematical studies of gravity currents composed of power-law fluids suggest that,  
794 although there may be some increase in far-field surface slope associated with such effects,  
795 flow over a rigid base nonetheless tends to produce a steep front (Gratton et al., 1999).  
796 Our result, that steep topographic gradients can form with a Newtonian rheology, therefore,  
797 suggests that steep-fronted mountain ranges do not constrain whether flow in the ductile  
798 part of the lithosphere occurs by diffusion or dislocation creep, and demonstrates that the  
799 presence of strong lower crust can explain first-order contrasts in topographic gradients.

800

## 801 **6 Conclusion**

802 We have investigated the role of lateral contrasts in lower crustal strength in controlling the  
803 shape and evolution of mountain ranges. In south-east Tibet, stable-isotope palaeoaltimetry  
804 suggests that parts of the topography may have been at, or near, their present-day elevations  
805 since the late Eocene and that uplift is likely to have occurred more slowly than had pre-  
806 viously been inferred. In combination with a simple model, these results demonstrate that  
807 lateral strength contrasts are sufficient to explain first-order features of the deformation and  
808 topographic evolution in south-east Tibet, without invoking a low-viscosity, lower-crustal  
809 channel. Since our models of topographic evolution in the presence of lateral lower-crustal  
810 strength contrasts allow us to reproduce the main features of the present day topography,  
811 strain-rate and velocity field in south-east Tibet, we suggest that lateral strength contrasts  
812 provide a first-order control on the temporal evolution and shape of mountain ranges. Our  
813 modelling also suggests that lateral contrasts in lower crustal strength provide an explanation  
814 for the correlation between cratons and the steep gradients on the edges of some mountain  
815 ranges.

## 816 **Acknowledgements**

817 C.P. would like to thank Thomasina Ball and Jerome Neufeld for helpful discussions. This  
818 work forms part of the NERC- and ESRC-funded project ‘Earthquakes without Frontiers’  
819 and was partially supported by the NERC large grant ‘Looking inside the Continents from  
820 Space’. C.P. is funded by a Junior Research Fellowship from Queens’ College, University of  
821 Cambridge and was funded by a NERC studentship for part of the research. Figures were

822 prepared using the GMT package (Wessel et al., 2013). No data was created for this research.  
823 Palaeoaltimetry data can be found in Hoke et al. (2014); Li et al. (2015); Xu et al. (2016);  
824 Tang et al. (2017); Gourbet et al. (2017); Wu et al. (2018). Earthquake focal mechanisms  
825 can be found in Copley (2008) (and references therein), Zhang et al. (2010), Li et al. (2011),  
826 Han et al. (2014), Bai et al. (2017), Han et al. (2018), the CMT catalogue (Dziewonski et al.,  
827 1981; Ekström et al., 2012) and the ISC-EHB catalogue (Engdahl et al., 1998; International  
828 Seismological Centre, 2016). GPS data in Figure 3 are from Zheng et al. (2017).

## A Time evolution of a viscous current

We solve a simplified form of the Stokes' flow equations, proposed by Pattyn (2003) for glaciers. The key simplifications made in deriving these equations from the Stokes' equations are: Airy isostatic compensation at the base of the crust (discussed in section 3.2) and that the horizontal gradients of vertical velocity do not dominate the force balance, i.e. the terms  $\frac{\partial w}{\partial x}$  and  $\frac{\partial w}{\partial y}$  are small in comparison to either  $\frac{\partial u}{\partial z}$  and  $\frac{\partial v}{\partial z}$ , or  $\frac{\partial v}{\partial x}$  and  $\frac{\partial u}{\partial y}$ . These horizontal derivatives of vertical velocities may become important immediately adjacent to the change in basal boundary condition (Schmalholz et al., 2014). However, Pattyn (2003) demonstrated that the effect of these gradients being large is confined to a region over similar lateral extent to the thickness of the deforming layer (1–2 grid cells in our model), and that this does not affect the overall behaviour of the model. Neglecting these derivatives does not imply that the vertical velocities cannot vary horizontally, only that they do not dominate the balance of forces driving the flow.

We follow Pattyn in scaling the vertical dimension at each timestep (cf. his equation 44). We then solve the resulting velocity equations at each timestep (subject to the boundary conditions discussed below and in section 3.3) using the generalised minimum residual method (Saad and Schultz, 1986, in sparskit2).

The equations presented by Pattyn (2003) are for general, variable viscosity case, and these are the equations we solve in our modelling. However, since we consider the constant viscosity case here,  $\nabla\eta = \mathbf{0}$  and the unscaled velocity equations (15 and 16 in Pattyn, 2003) could be simplified to

$$\eta \left( 4 \frac{\partial^2}{\partial x^2} + \frac{\partial^2}{\partial y^2} + \frac{\partial^2}{\partial z^2} \right) u = \rho g \frac{\partial s}{\partial x} - 3\eta \frac{\partial^2 v}{\partial x \partial y} \quad (\text{A.1})$$

and

$$\eta \left( \frac{\partial^2}{\partial x^2} + 4 \frac{\partial^2}{\partial y^2} + \frac{\partial^2}{\partial z^2} \right) v = \rho g \frac{\partial s}{\partial y} - 3\eta \frac{\partial^2 u}{\partial x \partial y}. \quad (\text{A.2})$$

Taking partial derivatives of the incompressibility condition,

$$\frac{\partial u}{\partial x} + \frac{\partial v}{\partial y} + \frac{\partial w}{\partial z} = 0, \quad (\text{A.3})$$

with respect to  $x$  and  $y$ , and using the assumption that  $\frac{\partial w}{\partial x}$  and  $\frac{\partial w}{\partial y}$  are small in comparison to other velocity gradients, gives

$$\frac{\partial^2 u}{\partial x^2} + \frac{\partial^2 v}{\partial x \partial y} = 0, \quad (\text{A.4})$$

and

$$\frac{\partial^2 v}{\partial y^2} + \frac{\partial^2 u}{\partial y \partial x} = 0. \quad (\text{A.5})$$

Equations (A.1) and (A.2) then reduce to

$$\left( \frac{\partial^2}{\partial x^2} + \frac{\partial^2}{\partial y^2} + \frac{\partial^2}{\partial z^2} \right) u = \frac{\rho g}{\eta} \frac{\partial s}{\partial x} \quad (\text{A.6})$$

and

$$\left( \frac{\partial^2}{\partial x^2} + \frac{\partial^2}{\partial y^2} + \frac{\partial^2}{\partial z^2} \right) v = \frac{\rho g}{\eta} \frac{\partial s}{\partial y}. \quad (\text{A.7})$$

848

849

850

At each timestep we first solve for the horizontal velocities, then calculate the associated

851 evolution of the topography. From integrating the incompressibility condition (A.3) over the  
 852 layer thickness,  $H$  (Figure 4):

$$\frac{\partial H}{\partial t} = -\nabla_h \cdot (H\bar{u}, H\bar{v}), \quad (\text{A.8})$$

853 where bars denote vertical averaging, and

$$\nabla_h = \left( \frac{\partial}{\partial x}, \frac{\partial}{\partial y} \right). \quad (\text{A.9})$$

854 Equation (A.8) can be written as a diffusion equation for the topography. This approach  
 855 allows the diffusivities to be calculated on a staggered grid, preventing leapfrog instabilities  
 856 in the second-order finite differences. Pattyn (2003) expressed this diffusion equation as:

$$\frac{\partial H}{\partial t} = \nabla_h \cdot \left( D_x \frac{\partial H}{\partial x}, D_y \frac{\partial H}{\partial y} \right) + \nabla_h \cdot \left( D_x \frac{\partial b}{\partial x}, D_y \frac{\partial b}{\partial y} \right), \quad (\text{A.10})$$

(his equation 55, where we make the derivatives explicit here for clarity), and:

$$D_x = \left| \bar{u} H \left( \frac{\partial s}{\partial x} \right)^{-1} \right|,$$

$$D_y = \left| \bar{v} H \left( \frac{\partial s}{\partial y} \right)^{-1} \right|,$$

(the modulus signs were implied but not included in Pattyn, 2003). In the glacier case, for which this method was developed, there is no prescribed relationship between the surface height,  $s$ , and bed depth,  $b$  (although  $H = s - b$ ). However, for an isostatically-compensated fluid, such as the crust of south-east Tibet (e.g. Jordan and Watts, 2005),  $b = -fs$  and  $H = (1 + f)s$ , where  $f = \frac{\rho_c}{\rho_m - \rho_c}$ . For standard crust and mantle densities of  $2700 \text{ kg m}^{-3}$  and  $3300 \text{ kg m}^{-3}$  respectively,  $f = 4.5$ , which is what we assume here. Substituting these

relationships into (A.10) gives

$$\frac{\partial H}{\partial t} = \left( \frac{1}{f+1} \right) (\partial_x (D_x \partial_x H) + \partial_y (D_y \partial_y H)). \quad (\text{A.11})$$

We note that the diffusivities could alternatively have been defined as

$$D'_x = \left| \bar{u} H \left( \frac{\partial H}{\partial x} \right)^{-1} \right|,$$

$$D'_y = \left| \bar{v} H \left( \frac{\partial H}{\partial y} \right)^{-1} \right|,$$

in which case

$$\frac{\partial H}{\partial t} = (\partial_x (D'_x \partial_x H) + \partial_y (D'_y \partial_y H)). \quad (\text{A.12})$$

857  $D_n, n \in \{x, y\}$  becomes infinite if  $\frac{\partial s}{\partial n} = 0$ , but physically the topography in such regions  
 858 should not propagate (i.e.  $\frac{\partial H}{\partial t} = 0$ , since in regions of flat topography there are no pressure  
 859 contrasts to drive the flow). In such cases, therefore, we set  $D_n = 0$ .

860

861 We write equation (A.11) as a sparse matrix equation using a Crank-Nicolson scheme  
 862 for the finite differences, with diffusivities calculated on a staggered grid, the approach  
 863 suggested by Pattyn (2003). Solving both x and y terms in the same linear system, rather  
 864 than separating the components, gives better stability but means that the matrix does not  
 865 have a simple form (the separated case is tridiagonal, which was the form used by Reynolds  
 866 et al., 2015). We therefore solve this sparse system using the generalised minimum residual  
 867 method (Saad and Schultz, 1986).

868 **Boundary Conditions**

869 **Pressure Boundary conditions**

870 We use a constant height boundary condition on  $y = 0$ , where fluid enters the model domain  
871 (section 3.3). Since we solve the velocity equations separately from those for the topography  
872 (as discussed in the previous section of the appendix), we also require velocity boundary  
873 conditions consistent with there being no height change on this boundary through time.  
874 The computational cost involved in iterating between the height and velocity calculations  
875 in order to obtain the consistent boundary condition for the velocity is prohibitive, so we  
876 instead use a physically-motivated approximation, which we now describe.

877

Noting that the NW and SE margins of the region we study are isostatically compensated (e.g. Jordan and Watts, 2005), we impose the deviatoric stress resulting from integrated pressure differences between fluid in the domain and an undeforming reservoir outside the domain on  $y \in \{0, y_{max}\}$  and  $x \in \{0, x_{max}\}$  for  $y > y_b$  (where  $y_b$  denotes the far end of the basin, Figure 4). The horizontal driving force exerted by a column of thickness  $H_0$  on a column with thickness  $H = H_0 - \Delta H$ , where  $\Delta H$  is the difference in thickness between the two columns, is

$$\begin{aligned} \int_{-b}^s \Delta p \, dz &= -\frac{g\rho_c}{2} \left(1 - \frac{\rho_c}{\rho_m}\right) (H_0^2 - (H_0 - \Delta H)^2) \\ &= -\frac{g\rho_c}{2(1+f)} \Delta H (2H_0 - \Delta H), \end{aligned} \tag{A.13}$$

878 (e.g. Artyushkov, 1973; Molnar and Tapponnier, 1978; Dalmayrac and Molnar, 1981; Molnar  
879 and Lyon-Caen, 1988; Turcotte and Schubert, 2014, Figure A.1), where  $p$  is the lithostatic  
880 pressure. On the influx ( $y = 0$ ) boundary  $H_0 = 65$  km (corresponding to 4.5 km surface



881 relief above 40 km thick crust). The associated vertically averaged normal stress is

$$\Delta\sigma_{yy} = \sigma_{yy} - p = -\frac{g\rho_c}{2H(1+f)}\Delta H(2H_0 - \Delta H), \quad (\text{A.14})$$

882 on boundaries in  $y$ . The deviatoric stress,

$$\sigma'_{yy} = \sigma_{yy} - \frac{1}{3}(P + \Delta\sigma_{xx} + P + \Delta\sigma_{yy} + P) \quad (\text{A.15})$$

883 (assuming that the vertical normal stress is just the lithostatic pressure, i.e. Airy isostatic  
 884 equilibrium, as discussed in section 3.2 and assumed in the derivation of the velocity equa-  
 885 tions). In the 2D case, Schmalholz et al. (2019) showed that  $\sigma'_{yy} = \frac{1}{2}\Delta\sigma_{yy}$ . In the 3D case,  
 886 we need to make an additional assumption about the value of  $\Delta\sigma_{xx}$ . On the influx boundary  
 887 ( $y = 0$ ) there is no gradient of topography in the  $x$  direction, so an appropriate and simple  
 888 assumption is  $\Delta\sigma_{xx} = 0$ , giving

$$\sigma'_{yy} = \frac{2}{3}\Delta\sigma_{yy} = 2\eta\frac{\partial v}{\partial y}. \quad (\text{A.16})$$

889 Note that we define tensional stresses as positive. In practice,  $\Delta H$  is very small ( $\ll 0.5$  km),  
 890 since it is the difference in thickness between two adjacent grid points in our model, so these  
 891 deviatoric stresses are close to 0. The aim of this boundary condition is to provide the small  
 892 deviatoric stress inside our model domain associated with differences in topography from  
 893 an assumed external reservoir of crust at constant elevation and with zero deviatoric stress,  
 894 which drives fluid into the model domain.

895

896 For the outflux boundaries, we assume that there is a reservoir of crust with zero de-  
 897 viatoric stress (i.e. at fixed elevation,  $H_0 = 40$  km) outside the model domain. Rather  
 898 than fixing the height of the topography we use these velocity boundary conditions with

899 equation A.12 for the evolution of the topography. We make the same assumption as on the  
900  $y = 0$  boundary, that  $\Delta\sigma_{xx} = 0$  on  $y = y_{max}$ , and equivalently that  $\Delta\sigma_{xx} = 0$  on  $y = y_{max}$   
901 on  $x = 0$  and  $x = x_{max}$  for  $y > y_b$ . These assumptions neglect the effects of topographic  
902 gradients parallel to these boundaries. Ideally, we would impose the stress condition on  
903 the outflux boundary anti-parallel to the direction of flow, to represent a uniform reser-  
904 voir of unthickened crust. We impose the pressure condition on the normal stress to avoid  
905 needing to iterate multiple times for each time-step, between the orientations of the veloc-  
906 ities and of the deviatoric stresses. As a result, these boundary conditions determine only  
907 the boundary-perpendicular velocities, and we require a further condition on the boundary-  
908 parallel velocities. For the influx boundary, we set  $u = 0$ . For the outflux boundaries we set  
909  $\frac{\partial v}{\partial x} = 0$  on  $x \in \{0, x_{max}\}$  and  $\frac{\partial u}{\partial y} = 0$  on  $y = y_{max}$ . Since the far-field part of the domain is  
910 not substantially thickened by the end of our modelling, velocities adjacent to these far-field  
911 boundaries are small and we expect that imposing the stresses anti-parallel to the flow would  
912 not substantially alter our results. The physically-motivated approximation described here is  
913 sufficient for our first-order models, where our focus is primarily on the different topographic  
914 gradients which develop as a result of lateral lower-crustal strength contrasts.

915

## 916 **Reflection Boundary conditions**

On  $x \in \{0, x_{max}\}$  we use reflection boundary conditions  $u = 0$ ,  $\frac{\partial v}{\partial x} = 0$  for  $y < y_b$ . We impose the condition on  $u$  directly. As shown above, for constant viscosity,  $v$  is given by equation (A.7), which can be further simplified by considering

$$u|_{x=0} = 0 \Rightarrow \left. \frac{\partial u}{\partial y} \right|_{x=0} = 0 \Rightarrow \frac{\partial^2 u}{\partial x \partial y} = 0,$$

which, from (A.5), implies that  $\frac{\partial^2 v}{\partial y^2} = 0$ . Equation (A.7) therefore reduces to

$$\left( \frac{\partial^2}{\partial x^2} + \frac{\partial^2}{\partial z^2} \right) v = \frac{\rho g}{\eta} \frac{\partial s}{\partial y}, \quad (\text{A.17})$$

917 which we solve in its co-ordinate transformed form.

## 918 **References**

- 919 Allmann, B. P. and Shearer, P. M. (2009). Global variations of stress drop for moderate to  
920 large earthquakes. *J. Geophys. Res. Solid Earth*, 114(1):1–22.
- 921 Artyushkov, E. V. (1973). Stresses in the lithosphere caused by crustal thickness inhomog-  
922 eneities. *J. Geophys. Res.*, 78(32):7675–7708.
- 923 Bai, L., Li, G., Khan, N. G., Zhao, J., and Ding, L. (2017). Focal depths and mechanisms  
924 of shallow earthquakes in the Himalayan-Tibetan region. *Gondwana Res.*, 41:390–399.
- 925 Ball, T. V., Penney, C. E., Neufeld, J. A., and Copley, A. C. (2019). Controls on the  
926 geometry and evolution of thin-skinned fold-thrust belts, and applications to the Makran  
927 accretionary prism and Indo–Burman Ranges. *Geophys. J. Int.*, 218(1):247–267.
- 928 Beaumont, C., Jamieson, R. A., Nguyen, M. H., and Lee, B. (2001). Himalayan tecton-  
929 ics explained by extrusion of a low-viscosity crustal channel coupled to focused surface  
930 denudation. *Nature*, 414(6865):738–742.
- 931 Bischoff, S. and Flesch, L. (2019). Impact of Lithospheric Strength Distribution on India-  
932 Eurasia Deformation From 3-D Geodynamic Models. *J. Geophys. Res. Solid Earth*,  
933 124(1):1084–1105.
- 934 Burchfiel, B. C., Royden, L. H., van der Hilst, R. D., Hager, B. H., Chen, Z., King, R. W.,

- 935 Li, C., Lü, J., Yao, H., and Kirby, E. (2008). A geological and geophysical context for the  
936 Wenchuan earthquake of 12 May 2008, Sichuan, People's Republic of China. *GSA Today*,  
937 18(7):4.
- 938 Burchfiel, B. C., Zhiliang, C., Yupinc, L., and Royden, L. H. (1995). Tectonics of the  
939 Longmen Shan and Adjacent Regions, Central China. *Int. Geol. Rev.*, 37(8):661–735.
- 940 Bystricky, M. and Mackwell, S. (2001). Creep of dry clinopyroxene aggregates with defor-  
941 mation in the dislocation creep. *J. Geophys. Res.*, 106:13443–13454.
- 942 Chen, L., Gerya, T., Zhang, Z., Zhu, G., Duretz, T., and Jacoby, W. R. (2013a). Numerical  
943 modeling of eastern Tibetan-type margin: Influences of surface processes, lithospheric  
944 structure and crustal rheology. *Gondwana Res.*, 24(3-4):1091–1107.
- 945 Chen, L., Gerya, T. V., Zhang, Z. J., Aitken, A., Li, Z. H., and Liang, X. F. (2013b). For-  
946 mation mechanism of steep convergent intracontinental margins: Insights from numerical  
947 modeling. *Geophys. Res. Lett.*, 40(10):2000–2005.
- 948 Clark, M. K., Bush, J. W. M., and Royden, L. H. (2005a). Dynamic topography produced  
949 by lower crustal flow against rheological strength heterogeneities bordering the Tibetan  
950 Plateau. *Geophys. J. Int.*, 162:575–590.
- 951 Clark, M. K., House, M. A., Royden, L. H., Whipple, K. X., Burchfiel, B. C., Zhang, X., and  
952 Tang, W. (2005b). Late Cenozoic uplift of southeastern Tibet. *Geology*, 33(6):525–528.
- 953 Clark, M. K. and Royden, L. H. (2000). Topographic ooze: Building the eastern margin of  
954 Tibet by lower crustal flow. *Geology*, 28(8):703.
- 955 Clark, M. K., Royden, L. H., Whipple, K. X., Burchfiel, B. C., Zhang, X., and Tang, W.  
956 (2006). Use of a regional, relict landscape to measure vertical deformation of the eastern  
957 Tibetan Plateau. *J. Geophys. Res. Earth Surf.*, 111:F03002.

- 958 Clark, M. K., Schoenbohm, L. M., Royden, L. H., Whipple, K. X., Burchfiel, B. C., Zhang,  
959 X., Tang, W., Wang, E., and Chen, L. (2004). Surface uplift, tectonics, and erosion of  
960 eastern Tibet from large-scale drainage patterns. *Tectonics*, 23:TC1006.
- 961 Cook, K. L. and Royden, L. H. (2008). The role of crustal strength variations in shaping  
962 orogenic plateaus, with application to Tibet. *J. Geophys. Res. Solid Earth*, 113(8):1–18.
- 963 Copley, A. (2008). Kinematics and dynamics of the southeastern margin of the Tibetan  
964 Plateau. *Geophys. J. Int.*, 174:1081–1100.
- 965 Copley, A., Avouac, J. P., and Royer, J. Y. (2010). India-Asia collision and the Cenozoic  
966 slowdown of the Indian plate: Implications for the forces driving plate motions. *J. Geophys.  
967 Res. Solid Earth*, 115(3):1–14.
- 968 Copley, A. and McKenzie, D. (2007). Models of crustal flow in the India-Asia collision zone.  
969 *Geophys. J. Int.*, 169:683–698.
- 970 Culling, W. E. H. (1960). Analytical Theory of Erosion. *J. Geol.*, 68(3):336–344.
- 971 Dalmayrac, B. and Molnar, P. (1981). Parallel thrust and normal faulting in Peru and  
972 constraints on the state of stress. *Earth Planet. Sci. Lett.*, 55:473–481.
- 973 Dayem, K. E., Houseman, G. A., and Molnar, P. (2009a). Localization of shear along a  
974 lithospheric strength discontinuity: Application of a continuous deformation model to the  
975 boundary between Tibet and the Tarim Basin. *Tectonics*, 28(3):1–15.
- 976 Dayem, K. E., Molnar, P., Clark, M. K., and Houseman, G. A. (2009b). Far-field lithospheric  
977 deformation in Tibet during continental collision. *Tectonics*, 28(6):1–9.
- 978 Dziewonski, A. M., Chou, T., and Woodhouse, J. H. (1981). Determination of earthquake  
979 source parameters from waveform data for studies of global and regional seismicity. *J.  
980 Geophys. Res.*, 86(B4):2825–2852.

- 981 Ekström, G., Nettles, M., and Dziewoński, A. M. (2012). The global CMT project 2004-2010:  
982 Centroid-moment tensors for 13,017 earthquakes. *Phys. Earth Planet. Inter.*, 200-201:1–9.
- 983 Engdahl, E. R., van der Hilst, R., and Buland, R. (1998). Global teleseismic earthquake  
984 relocation with improved travel times and procedures for depth determination. *Bull.*  
985 *Seismol. Soc. Am.*, 88(3):722–743.
- 986 England, P. and Houseman, G. (1985). Role of lithospheric strength heterogeneities in the  
987 tectonics of Tibet and neighbouring regions. *Nature*, 315:297–301.
- 988 England, P. and Houseman, G. (1986). Finite strain calculations of continental deforma-  
989 tion: 2. Comparison with the India-Asia Collision Zone. *J. Geophys. Res. Solid Earth*,  
990 91(B3):3664–3676.
- 991 England, P. and McKenzie, D. (1982). A thin viscous sheet model for continental deforma-  
992 tion. *Geophys. J. Int.*, 70:295–321.
- 993 England, P. and McKenzie, D. (1983). Correction to: a thin viscous sheet model for conti-  
994 nental deformation. *Geophys. J. R. Astr. Soc.*, 73:523–532.
- 995 Fagereng, Å. and Biggs, J. (2019). New perspectives on ‘geological strain rates’ calculated  
996 from both naturally deformed and actively deforming rocks. *J. Struct. Geol.*, 125(January  
997 2018):100–110.
- 998 Fielding, E. J. and McKenzie, D. (2012). Lithospheric flexure in the Sichuan Basin and  
999 Longmen Shan at the eastern edge of Tibet. *Geophys. Res. Lett.*, 39:L09311.
- 1000 Flesch, L., Bendick, R., and Bischoff, S. (2018). Limitations on Inferring 3D Architecture  
1001 and Dynamics From Surface Velocities in the India-Eurasia Collision Zone. *Geophys. Res.*  
1002 *Lett.*, 45:1379–1386.

- 1003 Flesch, L. M., Haines, J. A., and Holt, W. E. (2001). Dynamics of the India-Eurasia Short-  
1004 ening. *J. Geophys. Res.*, 106(B8):16,435–16,460.
- 1005 Gourbet, L., Hervé, P., Paquette, J.-L., Sorrel, P., Maheo, G., Wang, G., Yadong, X.,  
1006 Cao, K., Antoine, P.-O., Eymard, I., Liu, W., Lu, H., Replumaz, A., Chevalier, M.-L.,  
1007 Kexin, Z., Jing, W., and Shen, T. (2017). Reappraisal of the Jianchuan Cenozoic basin  
1008 stratigraphy and its implications on the SE Tibetan plateau evolution. *Tectonophysics*,  
1009 700-701:162–179.
- 1010 Gratton, J., Minotti, F., and Mahajan, S. M. (1999). Theory of creeping gravity currents of  
1011 a non-Newtonian liquid. *Phys. Rev. E - Stat. Physics, Plasmas, Fluids, Relat. Interdiscip.*  
1012 *Top.*, 60(6):6960–6967.
- 1013 Han, L., Cheng, J., An, Y., Fang, L., Jiang, C., Chen, B., Wu, Z., Liu, J., Xu, X., Liu, R.,  
1014 Yao, Z., Wang, C., and Wang, Y. (2018). Preliminary Report on the 8 August 2017 Ms  
1015 7.0 Jiuzhaigou, Sichuan, China, Earthquake. *Seismol. Res. Lett.*, 89(2A):557–569.
- 1016 Han, L., Zeng, X., Jiang, C., Ni, S., Zhang, H., and Long, F. (2014). Focal Mechanisms of  
1017 the 2013 Mw 6.6 Lushan, China Earthquake and High-Resolution Aftershock Relocations.  
1018 *Seismol. Res. Lett.*, 85(1):8–14.
- 1019 Hirth, G. and Kohlstedt, D. (2003). Rheology of the upper mantle and the mantle wedge:  
1020 A view from the experimentalists. *Geophys. Monogr. Ser.*, 138:83–105.
- 1021 Hoke, G. D. (2018). Geochronology transforms our view of how Tibet’s southeast margin  
1022 evolved. *Geology*, 46(1):95–96.
- 1023 Hoke, G. D., Liu-Zeng, J., Hren, M. T., Wissink, G. K., and Garzione, C. N. (2014). Stable  
1024 isotopes reveal high southeast Tibetan Plateau margin since the Paleogene. *Earth Planet.*  
1025 *Sci. Lett.*, 394:270–278.

- 1026 Holmes, A. (1965). *The Principles of Physical Geology*. Nelson, Edinburgh.
- 1027 Houseman, G. and England, P. (1986). Finite strain calculations of continental deformation.  
1028 1. Method and general results for convergence zones. *J. Geophys. Res.*, 91(B3):3651–3663.
- 1029 Hren, M. T., Bookhagen, B., Blisniuk, P. M., Booth, A. L., and Chamberlain, C. P. (2009).  
1030  $\delta^{18}\text{O}$  and  $\delta\text{D}$  of streamwaters across the Himalaya and Tibetan Plateau: Implications for  
1031 moisture sources and paleoelevation reconstructions. *Earth Planet. Sci. Lett.*, 288:20–32.
- 1032 Huang, M. H., Bürgmann, R., and Freed, A. M. (2014). Probing the lithospheric rheology  
1033 across the eastern margin of the Tibetan Plateau. *Earth Planet. Sci. Lett.*, 396:88–96.
- 1034 Hubbard, J. and Shaw, J. H. (2009). Uplift of the Longmen Shan and Tibetan plateau, and  
1035 the 2008 Wenchuan ( $M = 7.9$ ) earthquake. *Nature*, 458(7235):194–197.
- 1036 Hubbard, J., Shaw, J. H., and Klinger, Y. (2010). Structural setting of the 2008 Mw7.9  
1037 Wenchuan, China, earthquake. *Bull. Seismol. Soc. Am.*, 100(5B):2713–2735.
- 1038 Huppert, H. E. (1982). The propagation of two-dimensional and axisymmetric viscous gravity  
1039 currents over a rigid horizontal surface. *J. Fluid Mech.*, 121:43–58.
- 1040 International Seismological Centre (2016). EHB Bulletin.
- 1041 Jackson, J., McKenzie, D., Priestley, K., and Emmerson, B. (2008). New views on the  
1042 structure and rheology of the lithosphere. *J. Geol. Soc. London.*, 165:453–465.
- 1043 Jordan, T. A. and Watts, A. B. (2005). Gravity anomalies, flexure and the elastic thickness  
1044 structure of the India-Eurasia collisional system. *Earth Planet. Sci. Lett.*, 236(3-4):732–  
1045 750.
- 1046 Kanamori, H. and Anderson, D. (1975). Theoretical basis of some empirical relations in  
1047 seismology. *B. Seism. Soc. Am.*, 65(5):1073–1095.



- 1048 Kirby, E., Reiners, P. W., Krol, M. A., Whipple, K. X., Hodges, K. V., Farley, K. A., Tang,  
1049 W., and Chen, Z. (2002). Late Cenozoic evolution of the eastern margin of the Tibetan  
1050 Plateau: Inferences from  $^{40}\text{Ar}/^{39}\text{Ar}$  and (U-Th)/He thermochronology. *Tectonics*,  
1051 21(1):1001–1019.
- 1052 Koons, P. O. (1989). The topographic evolution of collisional mountain belts: a numerical  
1053 look at the Southern Alps, New Zealand. *Am. J. Sci.*, 289(9):1041–1069.
- 1054 Lamb, S. (2000). Active deformation in the Bolivian Andes, South America. *J. Geophys.*  
1055 *Res. Solid Earth*, 105(B11):25627–25653.
- 1056 Lebedev, S. and Nolet, G. (2003). Upper mantle beneath Southeast Asia from S velocity  
1057 tomography. *J. Geophys. Res. Solid Earth*, 108(B1).
- 1058 Lechmann, S. M., May, D. A., Kaus, B. J., and Schmalholz, S. M. (2011). Comparing  
1059 thin-sheet models with 3-D multilayer models for continental collision. *Geophys. J. Int.*,  
1060 187(1):10–33.
- 1061 Lechmann, S. M., Schmalholz, S. M., Hetényi, G., May, D. A., and Kaus, B. J. P. (2014).  
1062 Quantifying the impact of mechanical layering and underthrusting on the dynamics of the  
1063 modern India-Asia collisional system with 3-D numerical models. *J. Geophys. Res. Solid*  
1064 *Earth*, 119(1):616–644.
- 1065 Li, C. and Van Der Hilst, R. D. (2010). Structure of the upper mantle and transition  
1066 zone beneath Southeast Asia from traveltimes tomography. *J. Geophys. Res. Solid Earth*,  
1067 115(7):1–19.
- 1068 Li, S., Currie, B. S., Rowley, D. B., and Ingalls, M. (2015). Cenozoic paleoaltimetry of the  
1069 SE margin of the Tibetan Plateau: Constraints on the tectonic evolution of the region.  
1070 *Earth Planet. Sci. Lett.*, 432:415–424.

- 1071 Li, S., Su, T., Spicer, R. A., Xu, C., Sherlock, S., Halton, A., Hoke, G., Tian, Y., Zhang, S.,  
1072 Zhou, Z., Deng, C., and Zhu, R. (2020). Oligocene deformation of the Chuandian terrane  
1073 in the SE margin of the Tibetan Plateau related to the extrusion of Indochina. *Tectonics*,  
1074 pages 0–3.
- 1075 Li, Z., Elliott, J. R., Feng, W., Jackson, J. A., Parsons, B. E., and Walters, R. J. (2011).  
1076 The 2010 Mw 6.8 Yushu (Qinghai, China) earthquake: Constraints provided by InSAR  
1077 and body wave seismology. *J. Geophys. Res. Solid Earth*, 116:B10302.
- 1078 Licht, A., Botsyun, S., Littell, V., Sepulchre, P., Donnadieu, Y., Risi, C., Rugenstein, J.  
1079 K. C., Page, M., Huntington, K. W., and Nivet, G. D. (2019). Is Tibetan Plateau uplift  
1080 more recent than we thought? In *AGU Fall Meet. Abstr.*
- 1081 Licht, A., van Cappelle, M., Abels, H. A., Ladant, J.-B., Trabucho-Alexandre, J., France-  
1082 Lanord, C., Donnadieu, Y., Vandenberghe, J., Rigaudier, T., Lécuyer, C., Terry Jr, D.,  
1083 Adriaens, R., Boura, A., Guo, Z., Soe, A. N., Quade, J., Dupont-Nivet, G., and Jaeger,  
1084 J.-J. (2014). Asian monsoons in a late Eocene greenhouse world. *Nature*, 513(7519):501–  
1085 506.
- 1086 Liu, C. Z., Wu, F. Y., Sun, J., Chu, Z. Y., and Yu, X. H. (2013). Petrology, geochemistry  
1087 and ReOs isotopes of peridotite xenoliths from Maguan, Yunnan Province: Implications  
1088 for the Cenozoic mantle replacement in southwestern China. *Lithos*, 168-169:1–14.
- 1089 Liu, Q. Y., van der Hilst, R. D., Li, Y., Yao, H. J., Chen, J. H., Guo, B., Qi, S. H., Wang,  
1090 J., Huang, H., and Li, S. C. (2014). Eastward expansion of the Tibetan Plateau by crustal  
1091 flow and strain partitioning across faults. *Nat. Geosci.*, 7:361–365.
- 1092 Liu-Zeng, J., Tapponnier, P., Gaudemer, Y., and Ding, L. (2008). Quantifying landscape  
1093 differences across the Tibetan plateau: Implications for topographic relief evolution. *J.*  
1094 *Geophys. Res. Earth Surf.*, 113:F04018.

- 1095 Liu-Zeng, J., Zhang, J., McPhillips, D., Reiners, P., Wang, W., Pik, R., Zeng, L., Hoke, G.,  
1096 Xie, K., Xiao, P., Zheng, D., and Ge, Y. (2018). Multiple episodes of fast exhumation since  
1097 Cretaceous in southeast Tibet, revealed by low-temperature thermochronology. *Earth*  
1098 *Planet. Sci. Lett.*, 490:62–76.
- 1099 Maurin, T., Masson, F., Rangin, C., Min, U. T., and Collard, P. (2010). First global  
1100 positioning system results in northern Myanmar: Constant and localized slip rate along  
1101 the Sagaing fault. *Geology*, 38(7):591–594.
- 1102 McGroder, M. F., Lease, R. O., and Pearson, D. M. (2014). Along-strike variation in struc-  
1103 tural styles and hydrocarbon occurrences, Subandean fold-and-thrust belt and inner fore-  
1104 land, Colombia to Argentina. In *Geol. Soc. Am. Mem.*, volume 212, pages 79–113.
- 1105 McKenzie, D., Jackson, J., and Priestley, K. (2005). Thermal structure of oceanic and  
1106 continental lithosphere. *Earth Planet. Sci. Lett.*, 233:337–349.
- 1107 McKenzie, D., McKenzie, J., and Fairhead, D. (2019). The Mechanical Structure of Tibet.  
1108 *Geophys. J. Int.*, pages 950–969.
- 1109 McKenzie, D., Nimmo, F., Jackson, J. A., Gans, P. B., and Miller, E. L. (2000). Char-  
1110 acteristics and consequences of flow in the lower crust. *J. Geophys. Res. Solid Earth*,  
1111 105(B5):11029–11046.
- 1112 McKenzie, D. and Priestley, K. (2008). The influence of lithospheric thickness variations on  
1113 continental evolution. *Lithos*, 102:1–11.
- 1114 Medvedev, S. E. and Podladchikov, Y. Y. (1999a). New extended thin-sheet approximation  
1115 for geodynamic applications—I. Model formation. *Geophys. J. Int.*, 136(3):586–608.
- 1116 Medvedev, S. E. and Podladchikov, Y. Y. (1999b). New extended thin-sheet approximation

- 1117 for geodynamic applications-II. Two-dimensional examples. *Geophys. J. Int.*, 136(3):586–  
1118 608.
- 1119 Merle, O. and Guillier, B. (1989). The building of the Central Swiss Alps: an experimental  
1120 approach. *Tectonophysics*, 165(1-4):41–56.
- 1121 Miller, K. G., Fairbanks, R. G., and Mountain, G. S. (1987). Tertiary Oxygen Isotope  
1122 Synthesis, Sea Level History, and Continental Margin Erosion. *Paleoceanography*, 2(1):1–  
1123 19.
- 1124 Molnar, P. and Lyon-Caen, H. (1988). Some simple physical aspects of the support, structure,  
1125 and evolution of mountain belts. In *GSA Spec. Pap.*, volume 218, pages 179–208.
- 1126 Molnar, P. and Tapponnier, P. (1978). Active Tectonics of Tibet. *J. Geophys. Res.*, 83(B11).
- 1127 Nissen, E., Tatar, M., Jackson, J., and Allen, M. (2011). New views on earthquake faulting  
1128 in the Zagros fold-and-thrust belt of Iran. *Geophys. J. Int.*, 186:928–944.
- 1129 Pattyn, F. (2003). A new three-dimensional higher-order thermomechanical ice sheet model:  
1130 Basic sensitivity, ice stream development, and ice flow across subglacial lakes. *J. Geophys.*  
1131 *Res.*, 108(B8):1–15.
- 1132 Pusok, A. E. and Kaus, B. J. P. (2015). Development of topography in 3-D continental-  
1133 collision models. *Geochemistry, Geophysics, Geosystems*, 16(5):1378–1400.
- 1134 Ramberg, H. (1981). The role of gravity in orogenic belts. *Geol. Soc. Spec. Publ.*, 9:125–140.
- 1135 Reynolds, K., Copley, A., and Hussain, E. (2015). Evolution and dynamics of a fold-thrust  
1136 belt: The Sulaiman Range of Pakistan. *Geophys. J. Int.*, 201:683–710.
- 1137 Richardson, N. J., Densmore, A. L., Seward, D., Fowler, A., Wipf, M., Ellis, M. A., Yong,  
1138 L., and Zhang, Y. (2008). Extraordinary denudation in the Sichuan Basin: Insights from

- 1139 low-temperature thermochronology adjacent to the eastern margin of the Tibetan Plateau.  
1140 *J. Geophys. Res. Solid Earth*, 113:B04409.
- 1141 Rowley, D. B. and Currie, B. S. (2006). Palaeo-altimetry of the late Eocene to Miocene  
1142 Lunpola basin, central Tibet. *Nature*, 439:677–681.
- 1143 Rowley, D. B., Pierrehumbert, R. T., and Currie, B. S. (2001). A new approach to stable  
1144 isotope-based paleoaltimetry: Implications for paleoaltimetry and paleohypsometry of the  
1145 High Himalaya since the late Miocene. *Earth Planet. Sci. Lett.*, 188:253–268.
- 1146 Royden, L. H., Burchfiel, B. C., King, R. W., Wang, E., Chen, Z., Shen, F., and Liu, Y.  
1147 (1997). Surface Deformation and Lower Crustal Flow in Eastern Tibet. *Science (80-. )*,  
1148 276(5313):788–790.
- 1149 Rybacki, E., Gottschalk, M., Wirth, R., and Dresen, G. (2006). Influence of water fugacity  
1150 and activation volume on the flow properties of fine-grained anorthite aggregates. *J.*  
1151 *Geophys. Res. Solid Earth*, 111(3).
- 1152 Saad, Y. and Schultz, M. H. (1986). GMRES: A Generalized Minimal Residual Algorithm  
1153 for Solving Nonsymmetric Linear Systems. *SIAM J. Sci. Stat. Comput.*, 7(3):856–869.
- 1154 Savin, S. M. (1977). The History of the Earth’s Surface Temperature During the Past 100  
1155 Million Years. *Annu. Rev. Earth Planet. Sci.*, 5(1):319–355.
- 1156 Schmalholz, S. M., Duretz, T., Hetenyi, G., and Medvedev, S. (2019). Distribution and  
1157 magnitude of stress due to lateral variation of gravitational potential energy between  
1158 Indian lowland and Tibetan plateau. *Geophys. J. Int.*, 216(2):1313–1333.
- 1159 Schmalholz, S. M., Medvedev, S., Lechmann, S. M., and Podladchikov, Y. (2014). Relation-  
1160 ship between tectonic overpressure, deviatoric stress, driving force, isostasy and gravita-  
1161 tional potential energy. *Geophys. J. Int.*, 197(2):680–696.

- 1162 Shen, Z. K., Lü, J., Wang, M., and Bürgmann, R. (2005). Contemporary crustal deformation  
1163 around the southeast borderland of the Tibetan Plateau. *J. Geophys. Res. Solid Earth*,  
1164 110:B11409.
- 1165 Sonder, L. J. and England, P. (1986). Vertical averages of rheology of the continental  
1166 lithosphere: relation to thin sheet parameters. *Earth Planet. Sci. Lett.*, 77:81–90.
- 1167 Steckler, M. S., Mondal, D. R., Akhter, S. H., Seeber, L., Feng, L., Gale, J., Hill, E. M., and  
1168 Howe, M. (2016). Locked and loading megathrust linked to active subduction beneath the  
1169 Indo-Burman Ranges. *Nat. Geosci.*, 9:615–618.
- 1170 Stocker, R. L. and Ashby, M. F. (1973). On the rheology of the upper mantle. *Rev. Geophys.*,  
1171 11(2):391–426.
- 1172 Stork, A. L., Selby, N. D., Heyburn, R., and Searle, M. P. (2008). Accurate relative earth-  
1173 quake hypocenters reveal structure of the Burma subduction zone. *Bull. Seismol. Soc.*  
1174 *Am.*, 98(6):2815–2827.
- 1175 Tang, M., Liu-Zeng, J., Hoke, G. D., Xu, Q., Wang, W., Li, Z., Zhang, J., and Wang, W.  
1176 (2017). Paleoelevation reconstruction of the Paleocene-Eocene Gonjo basin, SE-central  
1177 Tibet. *Tectonophysics*, 712-713:170–181.
- 1178 Turcotte, D. and Schubert, G. (2014). Body Forces and Surface Forces. In *Geodynamics*,  
1179 chapter 2, pages 93–98. Cambridge University Press, 3rd edition.
- 1180 Vilotte, J. P., Daignieres, M., Madariaga, R., and Zienkiewicz, O. C. (1984). The role of a  
1181 heterogeneous inclusion during continental collision. *Phys. Earth Planet. Inter.*, 36:236–  
1182 259.
- 1183 Wang, E. and Burchfiel, B. C. (1997). Interpretation of Cenozoic Tectonics in the Right-

- 1184 Lateral Accommodation Zone Between the Ailao Shan Shear Zone and the Eastern Hi-  
1185 malayan Syntaxis. *Int. Geol. Rev.*, 39(3):191–219.
- 1186 Wang, E., Kirby, E., Furlong, K. P., Van Soest, M., Xu, G., Shi, X., Kamp, P. J. J., and  
1187 Hodges, K. V. (2012). Two-phase growth of high topography in eastern Tibet during the  
1188 Cenozoic. *Nat. Geosci.*, 5:640–645.
- 1189 Wang, Y., Sieh, K., Tun, S. T., Lai, K.-Y., and Myint, T. (2014). Active tectonics and  
1190 earthquake potential of the Myanmar region. *J. Geophys. Res. Solid Earth*, 119:3767–  
1191 3822.
- 1192 Wang, Y., Zhang, B., Schoenbohm, L. M., Zhang, J., Zhou, R., Hou, J., and Ai, S. (2016).  
1193 Late Cenozoic tectonic evolution of the Ailao Shan-Red River fault (SE Tibet): Implica-  
1194 tions for kinematic change during plateau growth. *Tectonics*, 35:1969–1988.
- 1195 Wessel, P., Smith, W. H. F., Scharroo, R., Luis, J., and Wobbe, F. (2013). Generic Mapping  
1196 Tools: Improved version released. *EOS Trans. AGU*, 94(45):409–410.
- 1197 Wimpenny, S., Copley, A., Benavente Escobar, C. L., and Aguirre, E. (2018). Extension  
1198 and Dynamics of the Andes inferred from the 2016 Parina (Huarichancara) Earthquake.  
1199 *J. Geophys. Res. Solid Earth*, pages 1–31.
- 1200 Wittlinger, G., Vergne, J., Tapponnier, P., Farra, V., Poupinet, G., Jiang, M., Su, H.,  
1201 Herquel, G., and Paul, A. (2004). Teleseismic imaging of subducting lithosphere and  
1202 Moho offsets beneath western Tibet. *Earth Planet. Sci. Lett.*, 221(1-4):117–130.
- 1203 Wu, J., Zhang, K., Xu, Y., Wang, G., Garzzone, C. N., Eiler, J., Leloup, P. H., Sorrel, P.,  
1204 and Mahéo, G. (2018). Paleoelevations in the Jianchuan Basin of the southeastern Tibetan  
1205 Plateau based on stable isotope and pollen grain analyses. *Palaeogeogr. Palaeoclimatol.*  
1206 *Palaeoecol.*, 510(March):93–108.

- 1207 Xiong, Z., Ding, L., Spicer, R. A., Farnsworth, A., Wang, X., Valdes, P. J., Su, T., Zhang,  
1208 Q., Zhang, L., Cai, F., Wang, H., Li, Z., Song, P., Guo, X., and Yue, Y. (2020). The early  
1209 Eocene rise of the Gonjo Basin, SE Tibet: From low desert to high forest. *Earth Planet.*  
1210 *Sci. Lett.*, 543:116312.
- 1211 Xu, Q., Liu, X., and Ding, L. (2016). Miocene high-elevation landscape of the eastern  
1212 Tibetan Plateau. *Geochemistry, Geophys. Geosystems*, 17(10):4254–4267.
- 1213 Xu, X., Ding, Z., Shi, D., and Li, X. (2013). Receiver function analysis of crustal structure  
1214 beneath the eastern Tibetan plateau. *J. Asian Earth Sci.*, 73:121–127.
- 1215 Yang, R., Willett, S. D., and Goren, L. (2015). In situ low-relief landscape formation as a  
1216 result of river network disruption. *Nature*, 520:526–529.
- 1217 Yu, H. M., Lin, C. Y., Shi, L. B., Xu, J. D., and Chen, X. D. (2010). Characteristics and  
1218 origin of mafic and ultramafic xenoliths in trachyandesite lavas from Heikongshan volcano,  
1219 Tengchong, Yunnan Province, China. *Sci. China Earth Sci.*, 53(9):1295–1306.
- 1220 Zachos, J., Pagani, H., Sloan, L., Thomas, E., and Billups, K. (2001). Trends, rhythms, and  
1221 aberrations in global climate 65 Ma to present. *Science (80-. )*, 292(5517):686–693.
- 1222 Zhang, P.-Z., Wen, X.-Z., Shen, Z.-K., and Chen, J.-H. (2010). Oblique, High-Angle, Listric-  
1223 Reverse Faulting and Associated Development of Strain: The Wenchuan Earthquake of  
1224 May 12, 2008, Sichuan, China. *Annu. Rev. Earth Planet. Sci.*, 38(1):353–382.
- 1225 Zheng, G., Wang, H., Wright, T. J., Lou, Y., Zhang, R., Zhang, W., Shi, C., Huang, J., and  
1226 Wei, N. (2017). Crustal Deformation in the India-Eurasia Collision Zone From 25 Years  
1227 of GPS Measurements. *J. Geophys. Res. Solid Earth*, 122(11):9290–9312.



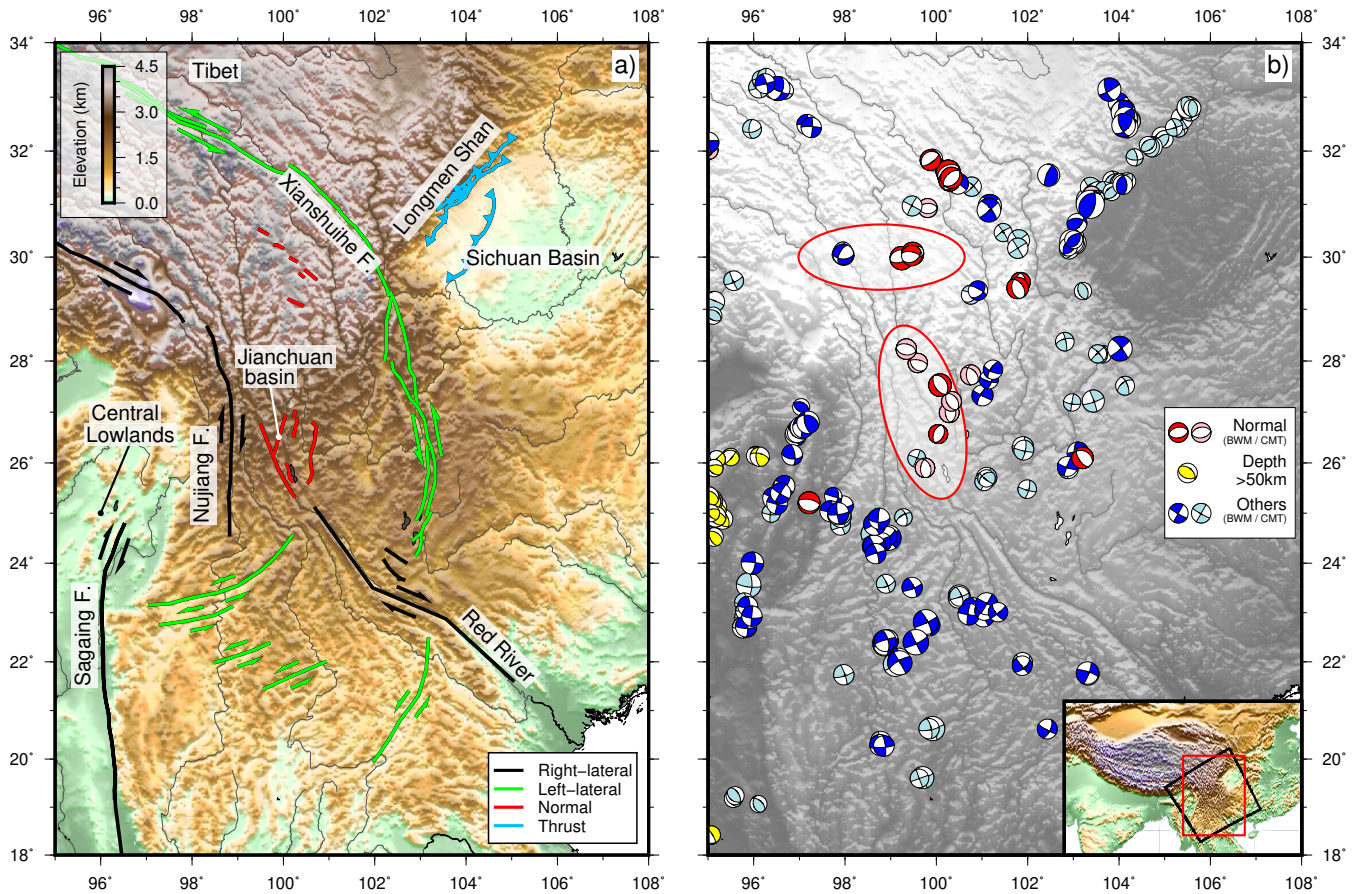


Figure 1: a) Major active faults in south-east Tibet, from Copley (2008); Hubbard and Shaw (2009). Black and green lines are right- and left-lateral strike-slip faults respectively. Note the opposite sense of shear adjacent to the Central Lowlands of Myanmar and Sichuan Basin. Red lines show normal faults. Blue lines show thrust faults with teeth on the hanging-wall side. b) Focal mechanisms of earthquakes in south-east Tibet. Focal mechanisms determined from body-waveform modelling from Copley (2008) (and references therein), Zhang et al. (2010), Li et al. (2011), Han et al. (2014), Bai et al. (2017), Han et al. (2018) are shown in red if they have a rake of  $-90\pm 35^\circ$  (normal faulting), and dark blue otherwise. Yellow focal mechanisms are  $>50$  km deep and are associated with subduction beneath the Indo-Burman ranges, most other earthquakes have depths less than  $\sim 20$  km. Focal mechanisms in pink (normal faulting, with rakes of  $-90\pm 35^\circ$ ) and pale blue are those from the CMT catalogue up to May 2016 with  $>70\%$  double couple and  $>10$  depth phases in the EHB catalogue if the earthquake occurred before 2009. Two regions of normal faulting discussed in the text are circled in red. Red box in inset shows the figure's location, black box shows location of Figure 3.

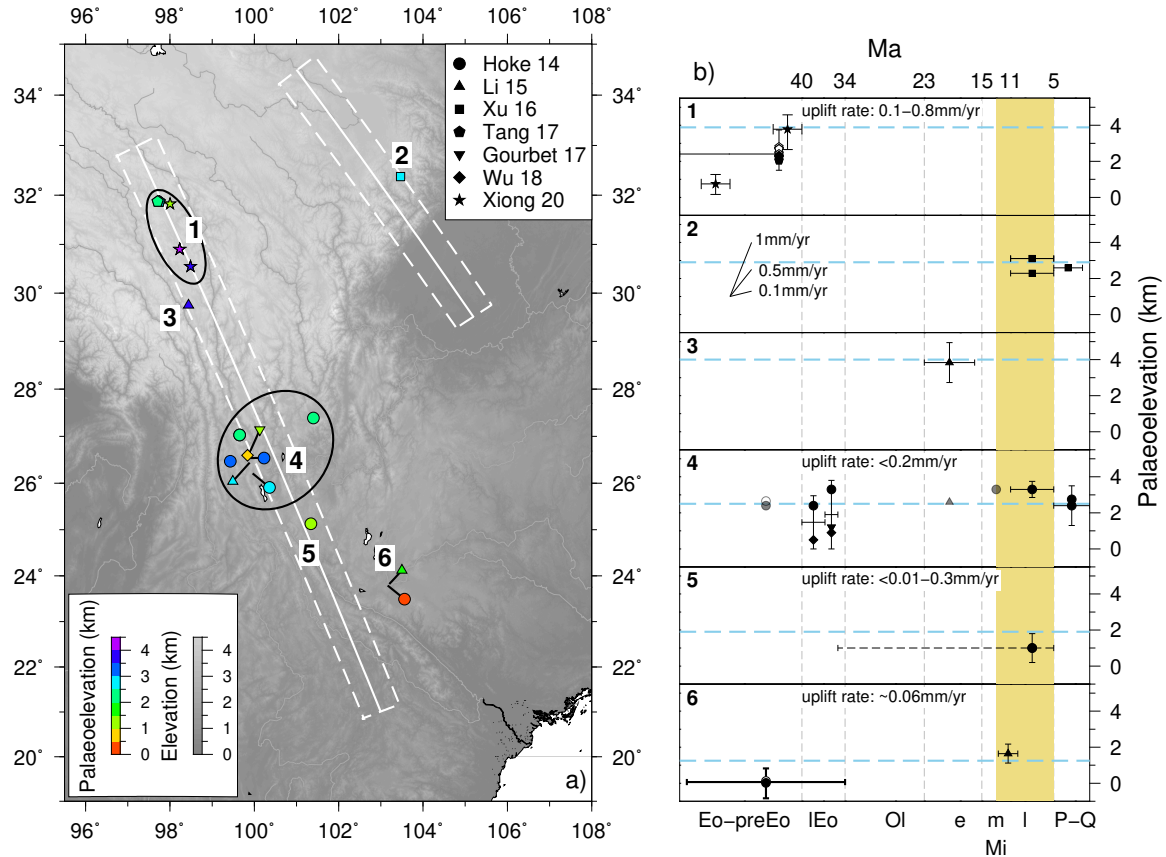


Figure 2: Results of stable-isotope palaeoaltimetry studies in south-east Tibet. a) Sample localities from Hoke et al. (2014); Li et al. (2015); Xu et al. (2016); Tang et al. (2017); Gourbet et al. (2017) and Wu et al. (2018) are coloured by palaeoelevation. 6 regions are labelled, which correspond to panels in b, ellipses indicate the extents of regions 1 (Gonjo Basin) & 4 (Jianchuan and surrounding basins). White lines and boxes show the regions plotted as topographic profiles in Figure 6g and h. b) Sample ages and palaeoelevations in each region. Epoch labels are – Eo-preEo: Eocene-pre Eocene >40 Ma, IEo: late Eocene: 40–34 Ma, Ol: Oligocene 34–23 Ma, eMi: early Miocene 23–15 Ma, mMi: middle Miocene 15–11 Ma, lMi: late Miocene 7–5 Ma, P-Q: Pliocene–Quaternary 5–0 Ma. Symbol shapes are as in a). Yellow bar shows the timing of increased exhumation and erosion rates suggested by Clark et al. (2005b) to indicate rapid uplift. Dashed blue lines indicate mean present-day sample-site elevation for each region. Where multiple samples from the same author are reported in the same epoch in the same region only a single error bar (representing the highest and lowest palaeoelevation estimates) is plotted. Palaeoelevation estimates using a modern temperature-elevation relationship are shown as filled symbols, those using a higher Eocene temperature estimate are unfilled. Gray points in region 4 are the authors' original palaeoelevation/age inferences. Black points in region 4 show the revised palaeoelevations/ages from Gourbet et al. (2017) and Wu et al. (2018), which we use to determine uplift rates. The age error bar in region 5 indicates the reassessment of Li et al. (2020) – those authors did not recalculate the palaeoelevation of the sample based on the revised dating.

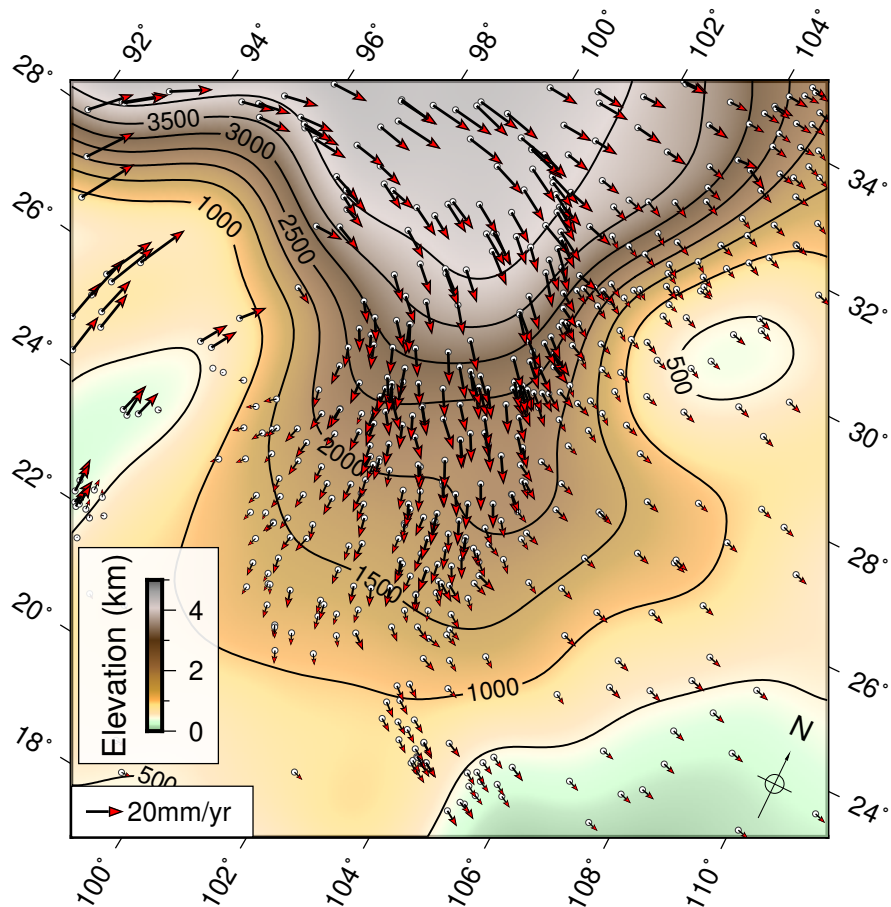


Figure 3: Topography of south-east Tibet after applying a low-pass 500 km-diameter Gaussian filter in an oblique Mercator projection (equator azimuth  $60^\circ$ , centred on  $101.5^\circ$  E,  $26.5^\circ$  N, location shown as black box in the inset of Figure 1b) for comparison to our model set-up (Figure 4) and results (Figures 5 and 8, Section 4). GPS velocities from Zheng et al. (2017) are shown in a Eurasia-fixed reference frame.

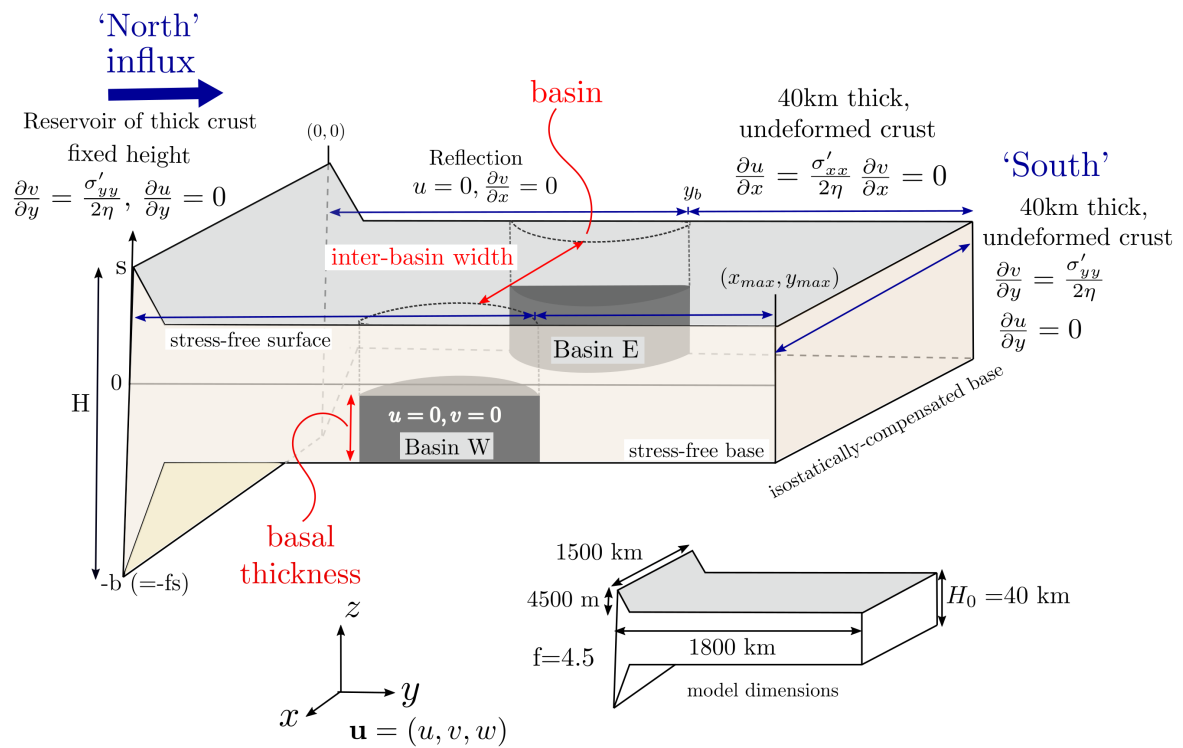


Figure 4: Model geometry, showing the initial topography and symmetric rigid regions. Boundary conditions on  $x = x_{max}$  are the same as those on  $x = 0$ . Inset shows dimensions of model domain. The isostatic root is not shown to scale.



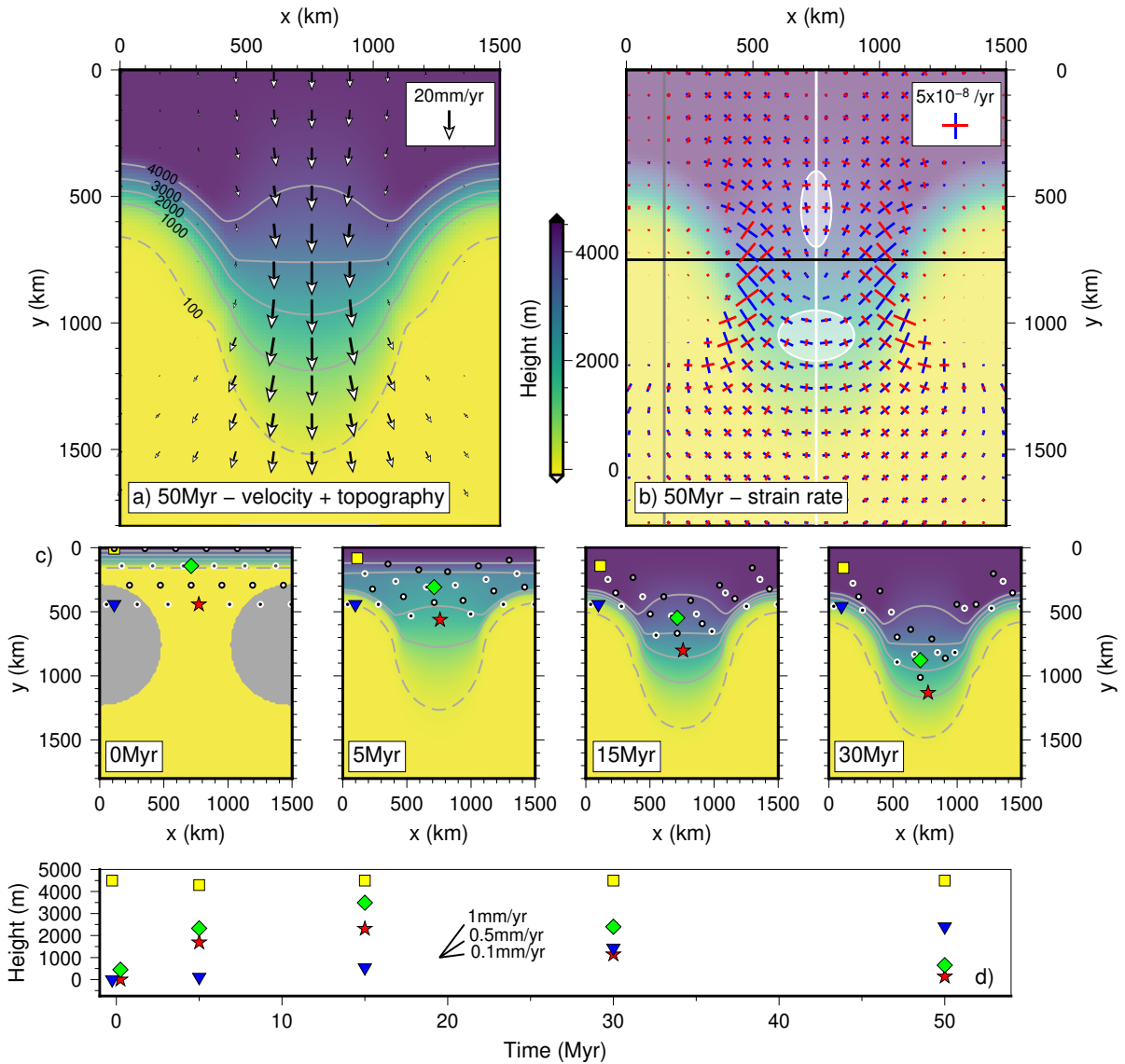


Figure 5: Modelling results for a symmetric model (both basins have the same size and location in  $y$ ) with 450 km-radius basins (grey semicircles at 0 Myr in c) with a 15 km-thick rigid base. The influx boundary (left-hand side in Figure 4) is at the top of each panel. a) topography and velocities after 50 Myr for a fluid with a viscosity of  $10^{22}$  Pas. Topography is plotted relative to the surface of 40 km-thick, isostatically-compensated crust and contoured at 100 m (dashed line), 1000 m, 2000 m, 3000 m and 4000 m. b) principal axes of the surface horizontal strain-rate tensor after 50 Myr. Blue bars are extensional, red bars are compressional. Gray, white and black lines show locations of profiles in Figures 6c, d and 7c respectively. White ellipses show the two regions where extensional strain rates are  $\sim 2$ –5 times greater than compressional strain rates, discussed in Section 5. c) Evolution of topography through time. Dots show large-scale lateral transport of particles moving with the surface of the current and can be viewed as analogous to the motion of near-surface carbonates used for palaeoaltimetry (Section 3.2). Contours are at 100 m (dashed line), 1000 m, 2000 m, 3000 m and 4000 m. d) shows the elevation history of the shaped particles

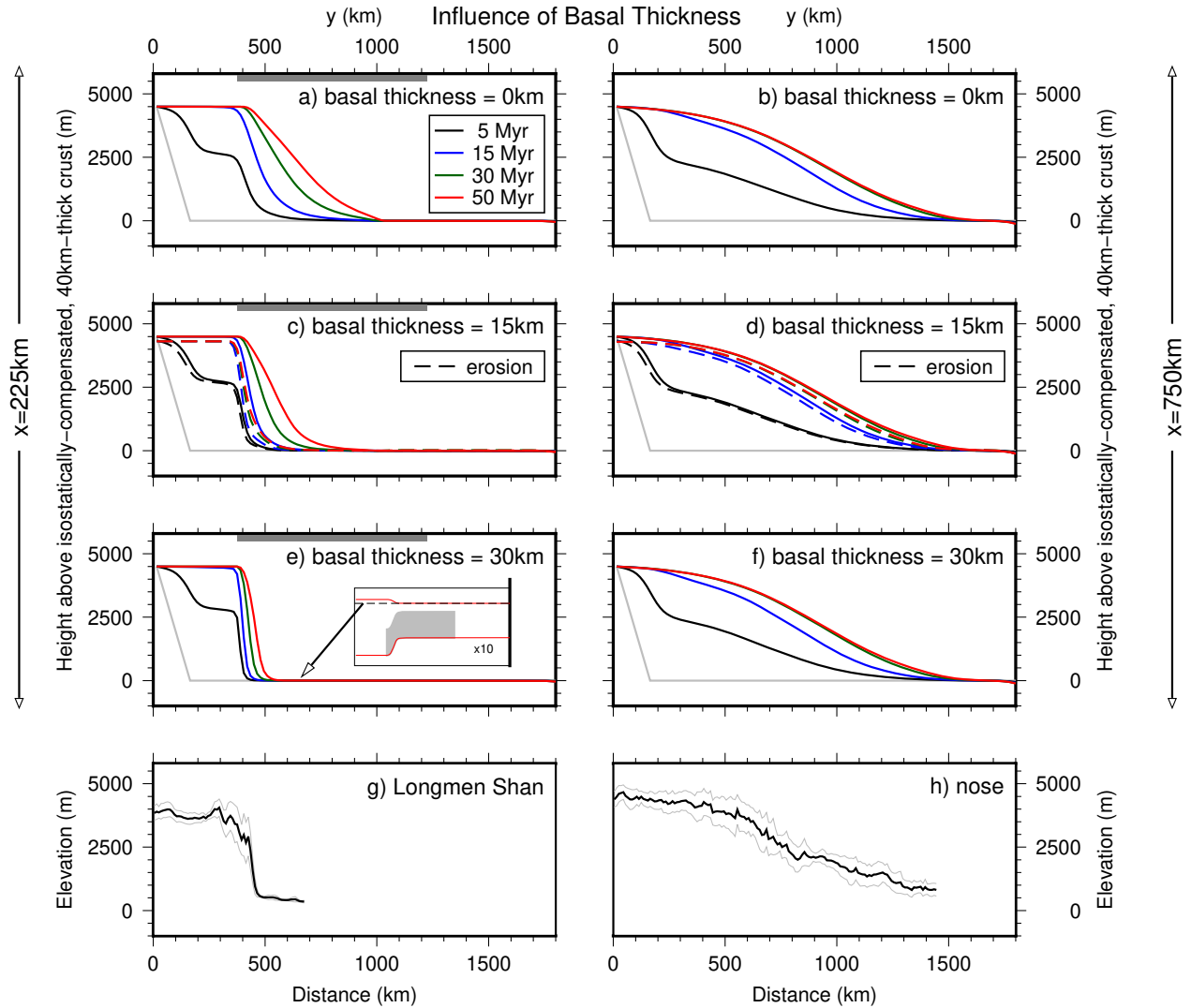


Figure 6: Effect of changing the basal thickness of the rigid basin (analogous to the thickness of undeforming lower crust) on the propagation of topography. The lateral extent of the basin which has a rigid basal thickness is indicated by the grey bars in a, c and e. a), c) and e) show profiles through the basin (gray line in Figure 5b) for basal thicknesses of 0 km (rigid base), 15 km and 30 km respectively. b), d) and f) show profiles through the inter-basin (stress-free base) region (white line in Figure 5b) for basal thicknesses of 0 km (rigid base), 15 km and 30 km respectively. The basal thickness has no significant effect on the development of topography in the regions with stress-free base. Elevations are relative to the surface of 40 km-thick, isostatically-compensated crust. Inset in e) shows the full thickness of the current (10x vertical exaggeration) to demonstrate how topography in this figure relates to full model. Grey region is the rigid basin. Dashed lines in c) and d) show the effect of erosion with  $\kappa = 4 \text{ mm yr}^{-1}$  in equation (1). c and d are profiles through the same model shown in Figure 5. g) and h) show topographic profiles and standard deviation across the Longmen Shan and between the Sichuan Basin and Central Lowlands of Myanmar respectively (profile locations shown in Figure 2a), demonstrating the similarity

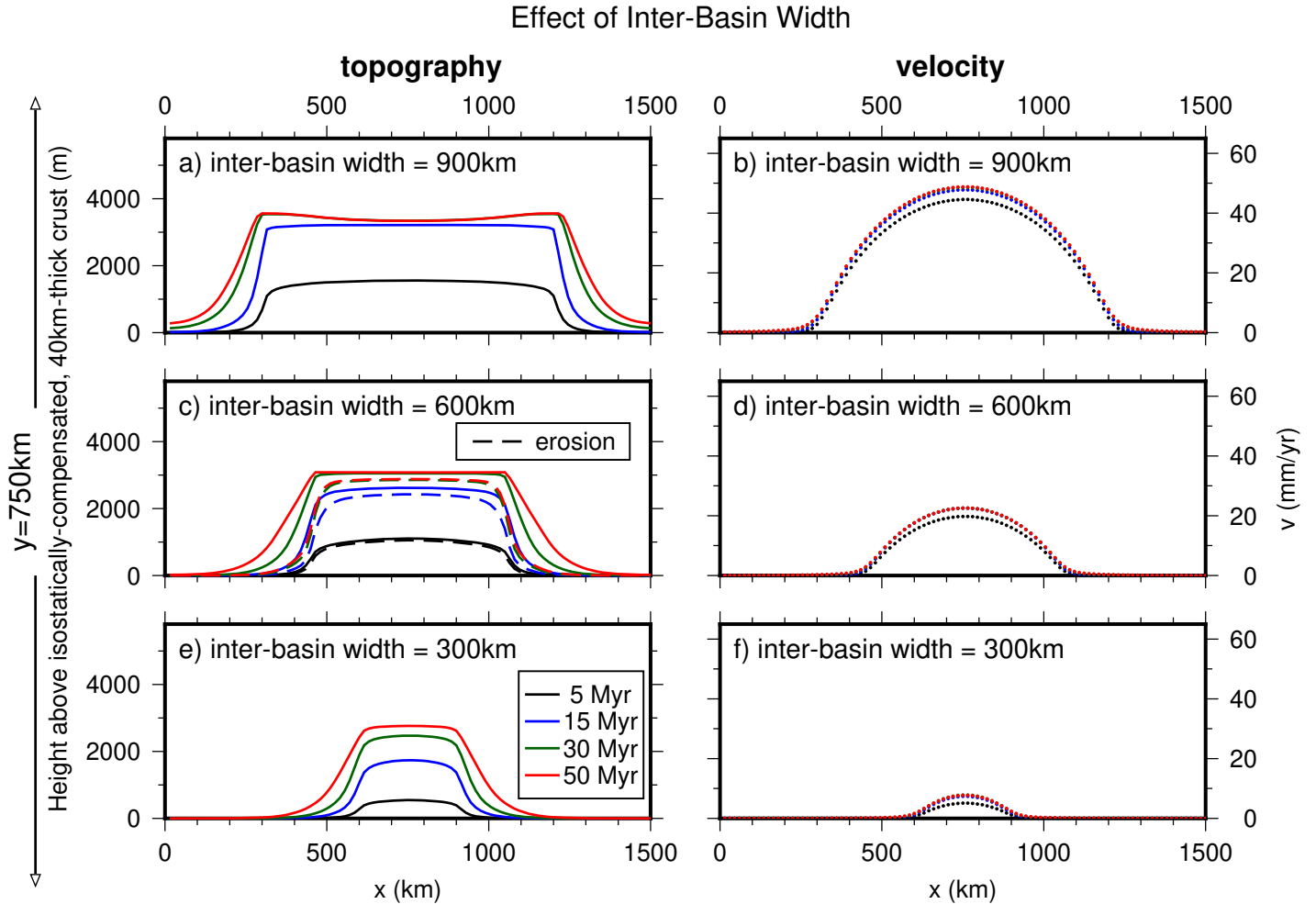


Figure 7: Effect of changing the distance between basins (inter-basin width, Figure 4). In each case profiles are taken at the centre of the semi-circular regions (black line in Figure 5b shows location of c and d), which have a basal thickness of 15 km. Elevations are relative to the surface of 40 km-thick, isostatically-compensated crust. a) and b) 900 km inter-basin width. a) shows the evolution of topography through time. The slight saddle arises because of thinning due to rapid velocities in the centre of the inter-basin region. b) the velocity perpendicular to the profile ( $v$  in Figure 4) after 50 Myr. c) and d) as for a and b but for an inter-basin width of 600 km. Note that c) and d) are profiles through the same model as Figure 5 and Figures 6c and d, with basin radius 450 km, inter-basin width 600 km and basal thickness 15 km. Dashed lines show the effects of erosion with  $\kappa = 4 \text{ mm yr}^{-1}$  in equation (1). e) and f) as for a and b but for an inter-basin width of 300 km.

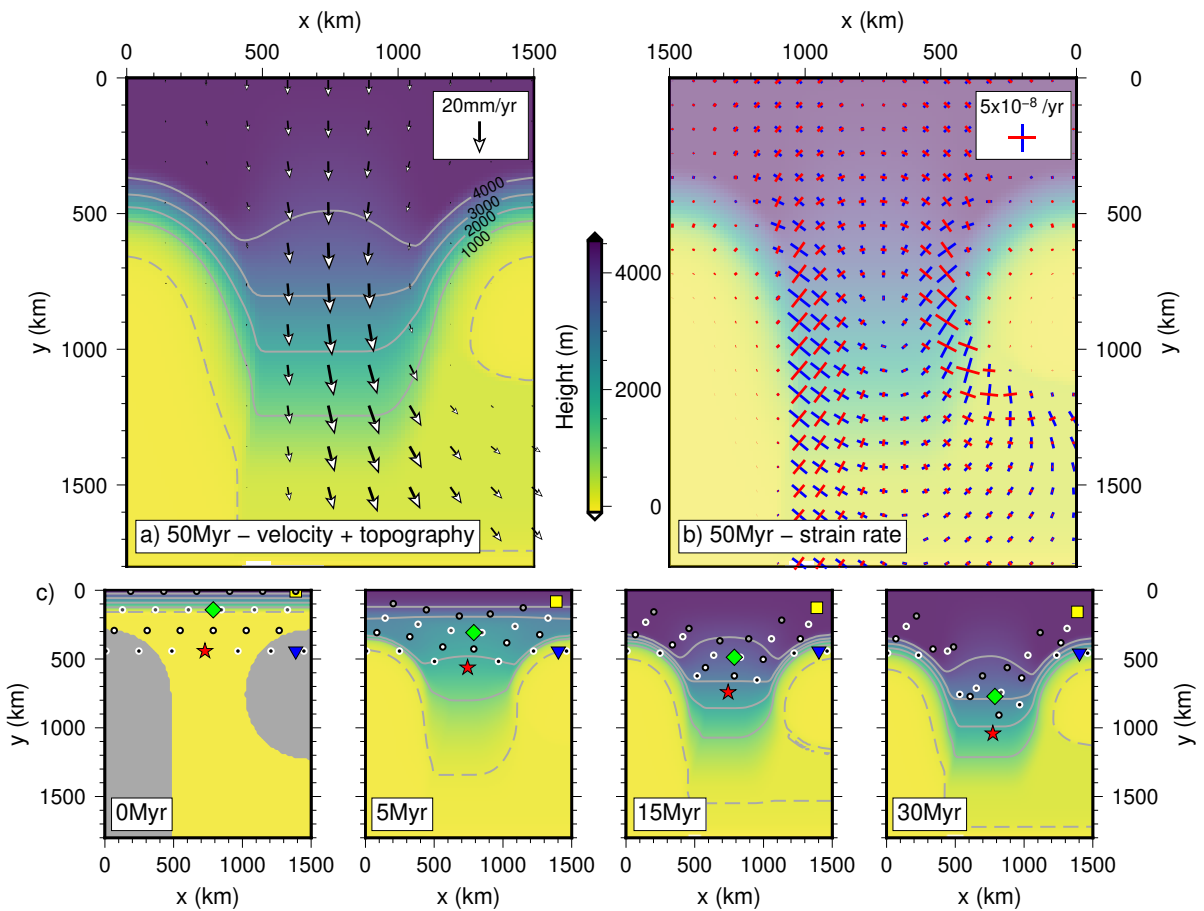


Figure 8: Modelling results for an asymmetric model set-up with 15 km basal thickness in the regions shown in grey in the 0 Myr panel of c. Panels are as for Figure 5. Note the broader region of shear adjacent to the extended basin.



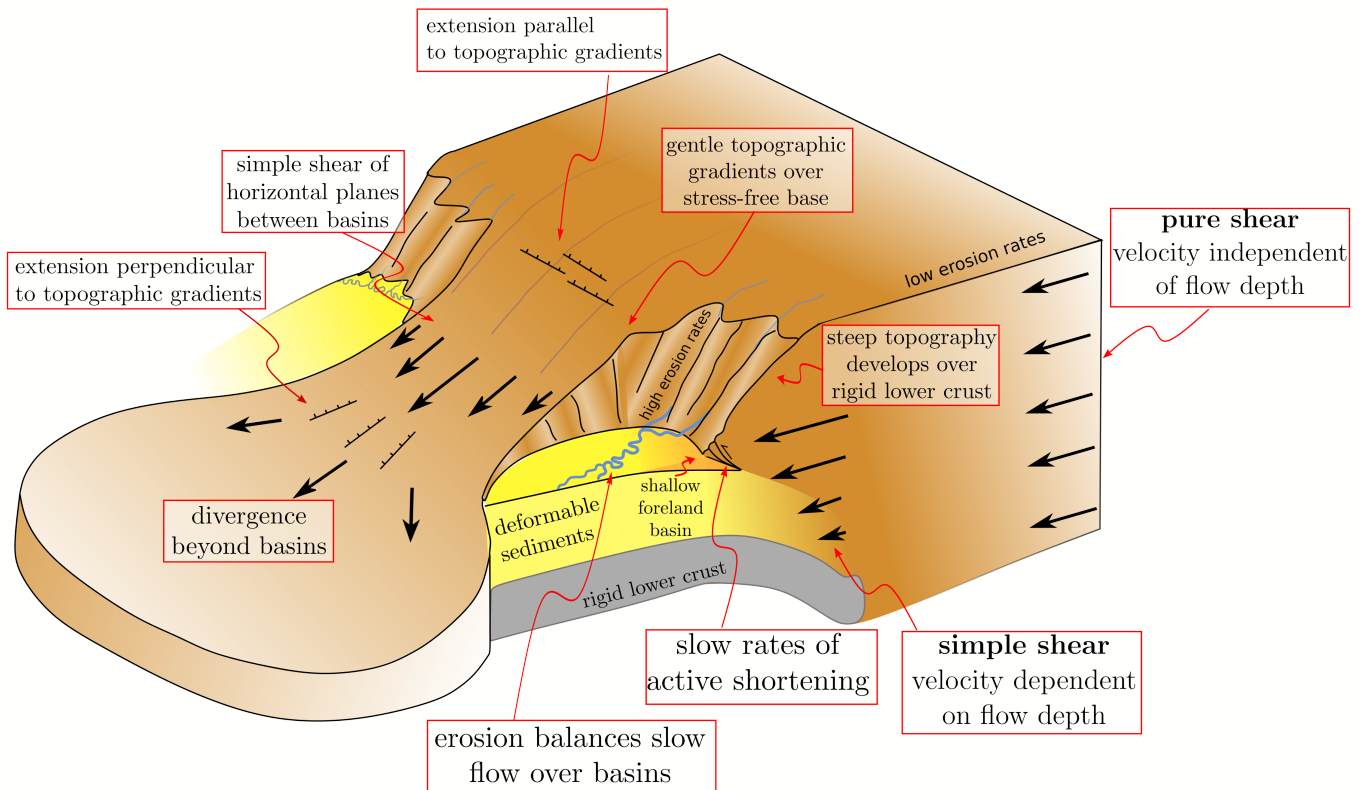


Figure 9: Cartoon showing effects of a rigid region on the development of topography. Steep topographic gradients develop above the region of rigid lower crust because of the dependence of velocity on flow depth. The compressional strain rates associated with growth of this step topography are much less than the shear strain rates between basins. Regions with a stress-free base (without strong lower crust) deform by pure shear of vertical planes, which results in gentle topographic gradients. Between two rigid regions flow is dominated by simple shear of horizontal planes, similar to flow in a pipe. Beyond the basins the flow can spread out, leading to extension.

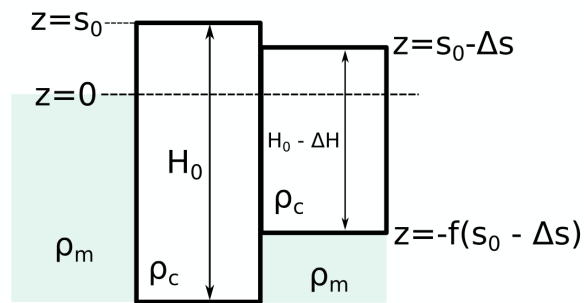


Figure A.1: Diagram to show isostatic balance used to find boundary conditions on  $x = 0, x_{max}$  for  $y > y_b$  and  $y = 0, y_{max}$ . The column of mantle on the left hand side of the figure is to demonstrate that the reference level is set by a column of mantle. The deviatoric stress between the two columns of continental crust is calculated as shown in the appendix.